CHALMERS
UNIVERSITY OF TECHNOLOGY

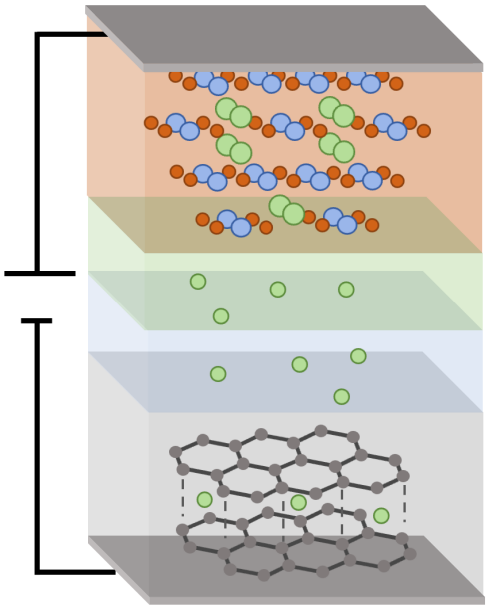

Dual electrolyte design for lithium-ion batteries

Extended electrochemical stability window by immiscible electrolytes

Master's thesis in Physics

SOFIA REINER

DEPARTMENT OF PHYSICS

CHALMERS UNIVERSITY OF TECHNOLOGY
Gothenburg, Sweden 2023
www.chalmers.se

Master's thesis 2023

Dual electrolyte design for lithium-ion batteries

Extended electrochemical stability window by immiscible electrolytes

SOFIA REINER

CHALMERS
UNIVERSITY OF TECHNOLOGY

Department of Physics
Division of Material Physics
Chalmers University of Technology
Gothenburg, Sweden 2023

Dual electrolyte design for lithium-ion batteries
Extended electrochemical stability window by
immiscible electrolytes
SOFIA REINER

Supervisor: Dr. Clément Pechberty, Department of Physics
Examiner: Prof. Patrik Johansson, Department of Physics

Master's Thesis 2023
Department of Physics
Division of Material Physics
Chalmers University of Technology
SE-412 96 Gothenburg
Telephone +46 31 772 1000

Cover: Schematic of a LNMO/graphite intercalating lithium-ion battery with two immiscible electrolytes.

Typeset in LaTeX
Printed by Chalmers Reproservice
Gothenburg, Sweden 2023

Dual electrolyte design for lithium-ion batteries
Extended electrochemical stability window by immiscible electrolytes
SOFIA REINER
Department of Physics
Chalmers University of Technology

Abstract

The lithium-ion battery is the fastest growing energy storage technology, and dominates in demand for smaller portable applications and electric vehicles due to its high energy density, small weight, and long lifespan. New developments in the materials used as positive electrodes enable the battery cells to operate under higher voltages than their predecessors, increasing the maximal energy contained. However, the voltage range of these cells extends beyond the reduction and oxidation limits of conventional electrolyte solvents, causing degradation and subsequent failure. In this work, a dual electrolyte concept is proposed and evaluated, in which each electrode has its own catered electrolyte, reducing the voltage window each electrolyte must be electrochemically stable in. Pairs of immiscible electrolytes consisting of both organic solvents and room temperature ionic liquids were evaluated and the diffusion between them in a cell setting was studied by Raman confocal spectroscopy, showing little diffusion of higher viscosity ionic liquids. Furthermore, the electrochemical properties of the electrolyte pairs were tested by galvanostatic cycling, using lithium manganese nickel oxide (LNMO) and graphite as the cathode and anode respectively. An interface between two immiscible electrolytes, constituted by an ionic liquid and an organosulfur compound on one side, and an ether and a fluorinated carbonate ester on the other, was shown to allow for adequate mobility of ions in order to cycle a cell.

Keywords: lithium-ion batteries, high voltage electrodes, LNMO, dual electrolytes, ionic liquids

Acknowledgements

First and foremost I would like to thank my supervisor Dr. Clément Pechberty for his guidance and patience in the lab. It has been a true pleasure working with him and getting to learn the ins and outs of battery research and cell characterisation. I would also like to thank my examinator Prof. Patrik Johansson for giving me the chance to work with his group and for introducing me to the world of batteries. There are many I would like to thank at the Material Physics division who gave me the warmest welcome and support during my thesis work. Sharing the lab, office, and especially fika with all of you wonderful people has been lovely. Thank you for showing me a supporting work environment and for your openness to discuss all my questions, whether it be on how to best approach my Raman measurements, how to navigate life in academia, and on which coffee machine to avoid in the lunch room. I would also like to add a special thank you to Morrow Batteries for graciously supplying the LNMO electrodes used in this work. Finally, I would like to thank my family and friends for their endless support during my time at Chalmers.

Sofia Reiner, Gothenburg, June 2023

List of Acronyms

The acronyms that have been used in this thesis are here listed in alphabetical order.

ATR-FTIR	Attenuated Total Reflectance Fourier-Transform Infrared Spectroscopy
CCD	Charged Coupled Device
CEI	Cathode Electrolyte Interphase
DBE	Dibutyl Ether
DEE	Diethyl Ether
DMC	Dimethyl Carbonate
DME	Dimethoxyethane
DMF	Dimethyl Formamide
DMSO	Dimethyl Sulfoxide
EC	Ethylene Carbonate
Emim	1-Ethyl-3-methylimidazolium
ESW	Electrochemical Stability Window
FEC	Fluoroethylene Carbonate
FSI	Bis(fluorosulfonyl)imide
FWHM	Full Width at Half Maximum
GC	Galvanostatic Cycling
IL	Ionic Liquid
Im	Imidazolium
IRC	Irreversible Capacity
LFP	Lithium Iron Phosphate
LIB	Lithium-Ion Battery
LNMO	Lithium Nickel Manganese Oxide
LSV	Linear Sweep Voltammetry
LTO	Lithium Titanate
PC	Polypropylene Carbonate
PYR	Pyrrolidinium
PYR14	1-Butyl-1-methylpyrrolidinium
RTIL	Room Temperature Ionic Liquids
SEI	Solid Electrolyte Interphase
TFSI	Bis(trifluoromethanesulfonyl)imide
TMS	Sulfolane

Contents

1
Introduction

The demand for batteries has increased rapidly, with forecasts predicting a yearly increase of 25-30% up until 2030 [1][2]. Significant efforts are made in both academia and industry to match the rapid growth of applications needing battery storage. Challenges include both grid applications and smaller appliances as well as vehicles. To enable the shift from fossil fuels to renewable energy sources, there is a need to develop higher energy density, longer-lasting, and more cost-effective battery technologies. Parallel to the development of new designs, new materials are progressively added to the EU critical raw materials list, signifying a high risk that these materials will be hard to come by in the near future. In 2023, nickel joined lithium and cobalt on the list while also being metals that constitute the basis of materials used in batteries [3]. Consequently, care needs to be taken when developing new materials and technologies that enable the batteries to have long lifecycles while being sustainable in the long run, both in terms of criticality and environmental impact.

The first versions of the lithium-ion battery (LIB) resembling the current battery setup, with a metal oxide cathode and carbon-based anode, were introduced in the early 1990s. In comparison to the already established lead-acid, nickel-cadmium and nickel-metal hydride batteries, the LIBs had higher energy density as well as a long cycle life [4][5]. The high specific energy has made them especially suitable for portable applications which also has helped propel the rapid development of LIB technologies. Today, LIBs dominate in demand in the automobile industry and this industry is expected to dictate in which direction battery research is headed [6].

1.1 Principle of lithium-ion batteries

Batteries enable the storage of chemical energy and consist of two or more electrochemical cells. The term *battery* is often used to describe the full layout of assembled cells with additional circuitry or components, while the cell describes the unit where electrochemical reactions take place. A first distinction can be made between batteries available in the market. Batteries that can only be discharged once are called *primary batteries*, while rechargeable batteries are called *secondary batteries*. A battery or cell can be charged by letting non-spontaneous chemical reactions take place when applying a voltage across the cell. Through spontaneous reactions the stored energy can later be extracted and used for applications connected as a load [5]. A simple electrochemical cell consists of two electrodes, a liquid electrolyte, a separator and two metallic conductive terminals, or collectors, as shown in a simple layout in Fig. 1.1. The chemical reactions that drive all cells are the reduction and oxidation,

or redox reactions, of different species. In LIBs, the charging process is driven by the oxidation of lithium stored in one electrode, the migration of free lithium ions through the electrolyte and the subsequent reduction of the ions into lithium at the opposite electrode. During discharge the opposite process takes place, and the lithium is once again returned to the original electrode, a lower energy state for the cell. The electrons freed in the oxidation reactions contribute to a current in the external circuit which can be utilised by a connected application. An electrode will either act as a cathode or anode depending on if the cell is charged or discharged. However by convention, the reducing electrode during discharge will always be called cathode, or alternatively the *positive electrode*.

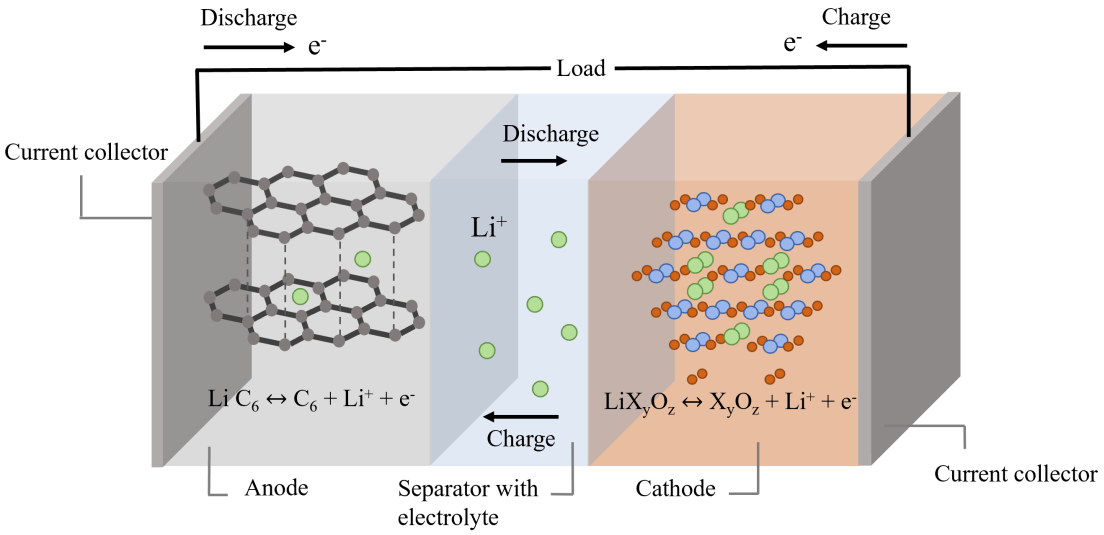

Figure 1.1: A simplified model of a typical intercalating LIB cell with a graphite anode and a transition metal oxide cathode, where X could for example be nickel, cobalt or manganese.

Both the cathode and anode need to be able to store and release lithium atoms. While there are multiple materials that have been found suitable as a cathode/anode pair for LIBs, the state-of-the-art cells consist of transition metal oxides as cathodes and graphite as an anode. They store the lithium atoms in interstitial sites in the atomic structure of the materials. In graphite, the lithium is intercalated between the sheets of graphene while the cathode materials have slightly different structures and interstitial sites depending on the chemical composition [5]. To ensure separation of ions and electrons and avoid unintentional cell discharge, the electrolyte must have high ionic conductivity with close to no electric conductivity. Commercial electrolytes are almost exclusively solid lithium salts dissolved in organic-based carbonate solvents [6][7]. However, other non-aqueous liquid electrolytes such as *room temperature ionic liquids* (RTIL), which are salts that are liquid at temperatures below 100° C, solid ceramics or semi-solid gel polymers are being developed and tested. The separator holding the electrolyte is a porous membrane that separates the electrodes, avoiding short circuiting. It is most often made of electrically

insulating materials such as polymers or glass fibres.

1.2 Electrochemical stability window of electrolytes

To properly intercalate the ions into the atomic structure of the electrodes, a high enough voltage needs to be applied between cathode and anode. Furthermore, this requires the electrolyte to be electrochemically stable against the electrodes of the batteries as well as on its own when placed under the operating voltage range of the battery. Outside of the *electrochemical stability window* (ESW), the electrolyte will start to oxidise or reduce and to decompose into new products. The decomposition would result in a decrease of lithium-ions taking part in the cycling process, leading to loss of cell capacity. Additionally, the properties of the product may not be desirable and may hinder the mobility of ions, subsequently leading to the failure of the cell. Considerable effort is therefore taken in battery research to develop new electrolyte solutions that extend the ESW or better caters to the operating voltage of the electrodes.

As an example, the standard operating voltage of the well-established cathode material lithium iron phosphate $LiFePO_4$ (LFP) is approximately 3.4 V, measured against a pure lithium metal counter electrode (vs. Li/Li^+) [8]. LFP is a commercially available material for both research and industry, and is especially favoured in the vehicle industry due to it being relatively inexpensive and lacking cobalt, a critical material that also has been connected to unethical mining [6][9]. The typical carbonate-based solvents used in electrolytes such as, ethylene carbonate (EC), propylene carbonate (PC) and dimethyl carbonate (DMC) have an oxidation limit $>$4.3 V vs. Li/Li^+, which well covers the operation voltage of LFP [10][11].

1.3 Dual electrolyte concepts for graphite/LNMO cells

Since the energy density of a cell is determined by the product of specific capacity and potential across the cell, high voltage positive electrodes are especially sought after and researched in industry and academia [10]. A promising cathode material currently in development is lithium-nickel-manganese-oxide $LiNi_{0.5}Mn_{1.5}O_4$ (LNMO) [6][10]. LNMO has a theoretical operating voltage of 4.7 V vs. Li/Li^+, well over the voltage of LFP, but unfortunately outside of the ESW of conventional electrolytes. As of the writing of this thesis, no commercial batteries based on LNMO material exist due to its poor cycling performance. It is however considered to be a part of the next generation of battery technologies [6].

Finding one single electrolyte with a wide enough ESW to accommodate both LNMO and the graphite anode has posed a challenge, leading to new battery concepts being investigated. The use of two different electrolytes in the same cell, catered to an electrode each and with an overlapping ESW to encompass the full voltage range of the cell, has been investigated in a few articles. To guarantee stability at each electrode the electrolytes must not mix and only be in contact with its

designated electrode. A proposed concept is the usage of an ion conductive membrane to avoid mixing but to let lithium ions pass through [12][13], which has been realised for a metal oxide cathode versus a silicon/graphite anode with Nafion as a membrane [12]. Another concept that has been realised for lithium-sulfur batteries is the use of dual electrolytes separated purely by the immiscibility of the liquids, with the goal of both extending the ESW and preventing certain compounds from crossing the cell [14][15]. However, to the best of the author's knowledge, no article to date has proposed a concept with dual electrolytes separated purely by chemical immiscibility for LIBs.

A proposed layout is presented with two separators, each soaked with a different electrolyte (Fig. 1.2). Assuming capillary forces are not enough to keep the electrolytes in the porous separators, the proposed layout demands that the cell is kept in a vertical position as well as the highest density electrolyte be on the bottom. Basic requirements for the dual electrolytes include their compatibility and stability with their respective electrode as well as having a good ionic conductivity both in the bulk but also across the electrolyte/electrolyte interface.

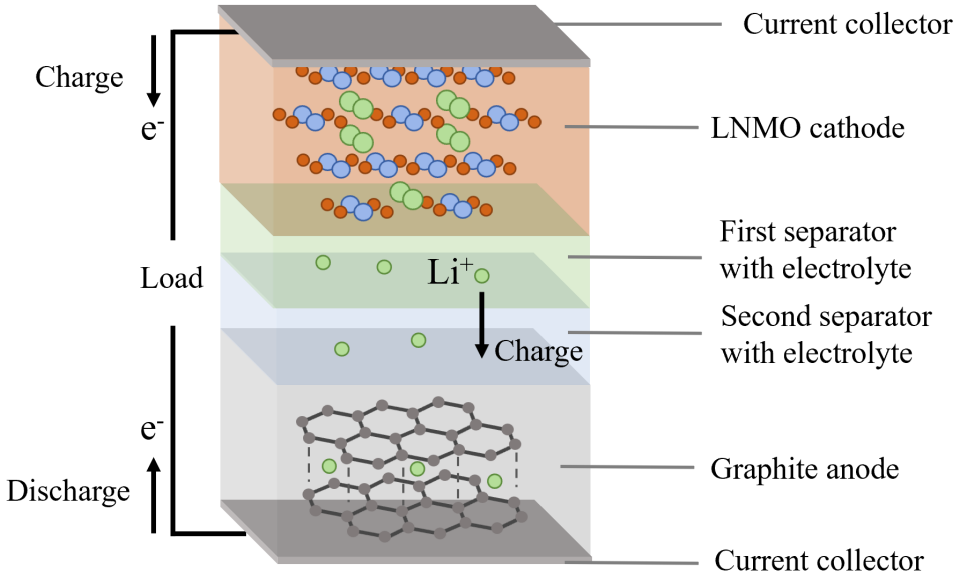

Figure 1.2: In the dual electrolyte concept two electrolytes would be used to cover the potential window and reach the operating voltage of the LNMO electrode. In this configuration, the electrolyte with the highest density should be placed on the bottom.

1.4 Aim and scope of thesis

The aim of this thesis is to investigate a dual electrolyte concept based on immiscible electrolytes and to explore the feasibility of creating a cell that can be reliably cycled. The diffusion of the electrolytes in the separators will be studied with Raman spectroscopy and the electrochemical properties by assembling pro-

totype batteries at the Material Physics department at Chalmers. With the goal being to find an electrolyte solution suitable for high voltage electrodes, the thesis will limit itself to working with LNMO and graphite as the cathode/anode pair. Furthermore, since the research concerning LIB electrolytes is such a vast area on its own and slightly out of the scope of this thesis, the focus will be placed on finding potential immiscible pairs comprised of electrolytes already well documented within LIB research and which are easily accessible. Given the contents of previously published work, this thesis will only include liquid non-aqueous electrolytes, including but not limited to, lithium salt in organic solvents, highly concentrated electrolytes and room-temperature ionic liquids or a combination of them. Where possible, extra care will be taken to choose sustainable and non-toxic materials and chemicals. Equally important is to choose electrolytes bearing the ecological effects in mind, e.g avoiding chemicals that could be harmful if accidentally released, to the greatest extent possible.

1.5 Thesis outline

Chapter 2 of this thesis gives a more thorough theoretical background to the chemical reactions taking place inside a lithium-ion cell as well as introducing the different categories of materials in LIBs and their properties. It concludes with the introduction of different cell configurations and how cells are tested within research. Next in Chapter 3, the immiscibility study of electrolytes is presented, commencing with a literary review of suitable electrolytes. There, the relevant theory of Raman spectroscopy is also presented, the chosen characterisation technique for investigating diffusion in the cell. The chapter ends with the results from a diffusion study performed on the separators and dual electrolyte pairs. Chapter 4 explains the basics of battery cell characterisation and battery cycling before discussing the electrochemical performance of the electrolytes in cells. Finally, in a finishing chapter, the dual electrolyte design is evaluated and discussed, while challenges and future outlooks on the design are presented.

2

Lithium-ion batteries

Initial interest in lithium as a material for battery applications is mainly attributed to its high reducing capability, its small ion/atom size and its low weight. The first batteries containing lithium can be found as far back as the 1910s, while the first cells based on intercalation mechanisms were introduced in the late 1970s. Finally, in the 1990s the modern LIB, with a lithium cobalt oxide cathode and a carbon anode, was released onto the commercial market fuelling the development of small portable devices due to its high energy density and relatively low price [4][16]. However, even though LIBs are increasingly gaining ground, some obstacles still stand in the way of them dominating the market of electric vehicles and grid applications in the same way as for portable electronics. The main issues are cost and availability of lithium, cobalt, and other materials in LIBs and not the theoretical limitations of the material [4][6]. Therefore, research into new cell concepts and optimisation of materials are as relevant as ever.

In this chapter, the basic electrochemistry of the LIB cell is presented along with the fundamentals of cell cycling and the underlying kinetics at the interfaces of the cell. The building blocks, the electrodes, electrolyte, and separator are thereafter introduced together with commonly used materials and their strengths and limitations. Finally, some experimental cell setups used in research for characterisation of battery materials are presented.

2.1 Redox reactions and electrochemistry of LIBs

As previously touched upon in the introduction, the chemical reactions occurring in a LIB cell are the reduction and oxidation of species at the interface between electrolyte and electrodes. In the case of the graphite/LNMO electrodes system, the reactions taking place during discharge at the two electrodes will be:

$$\text{Anode:} \qquad \mathrm{LiC_6} \leftrightarrow \mathrm{C_6} + \mathrm{Li^+} + \mathrm{e^-} \tag{2.1}$$

$$\text{Cathode:} \qquad \mathrm{Ni_{0.5}Mn_{1.5}O} + \mathrm{Li^+} + e^- \leftrightarrow \mathrm{LiNi_{0.5}\,Mn_{1.5}O} \tag{2.2}$$

Each of these reactions takes place between one of the electrodes and the electrolyte and are denoted as half-reactions. Together, these half-reactions give the total reaction of the full cell:

$$\mathrm{LiC_6} + \mathrm{Ni_{0.5}Mn_{1.5}} \leftrightarrow \mathrm{C_6} + \mathrm{LiNi_{0.5}\,Mn_{1.5}O} \tag{2.3}$$

The direction of this chemical reaction is driven by the system's tendency to always reduce the Gibbs free energy. This energy is related to the redox potential, or electromotive force, of the full cell E° by

$$\Delta G = -nFE^\circ, \tag{2.4}$$

where n is the number of electrons transferred between electrodes in moles and F is Faraday's constant, which gives the charge per mole. Intuitively, a larger potential difference across the cell will result in a higher thermodynamic driving force. The redox potential is also the difference between the individual reduction and oxidation potentials of the two electrodes measured in standard conditions. These voltages would be measured against a reference, typically the standard hydrogen electrode, in room temperature and with a standard concentration and pressure [17].

In a practical cell however, the conditions are rarely standard so adjustments to the calculations of the cell voltage must be done. When the cell is in equilibrium, meaning no direction is favoured in Eq. 2.3 and the net current is zero across the cell, the voltage can be described by the Nernst equation,

$$E = E^\circ - \frac{RT}{nF} \ln \frac{[\mathrm{C_6}]_A \, [\mathrm{LiNi_{0.5}Mn_{1.5}O_4}]_C}{[\mathrm{LiC_6}]_A \, [\mathrm{Ni_{0.5}Mn_{1.5}O_4}]_C} \tag{2.5}$$

where the brackets and subscripts indicate the activities of the species at either the anode or cathode, R is the gas constant and T is the temperature [17][18]. The activity of a species is proportional to the concentration of the species but corrects for the fact that particles of the species in a mixture do not behave like in an ideal mixture, meaning the mixture has the behaviour of an ideal gas. The correction is called the activity coefficient and will be different for each of the species inside the brackets in Equation 2.5. The equation makes it possible to approximate the redox potential of an assembled cell by using standard electrode potentials from data sheets and taking the concentrations in place of the activities [18].

A cell reaches its equilibrium state soon after assembly. Initially one direction of the reactions in Eq. 2.1 and 2.2 will be favoured and have a higher reaction rate. This leads to polarisation at the electrode/electrolyte interface due to the accumulation of charged particles involved in the reaction. This polarisation will work opposite to the initial potential difference, favouring the opposite reaction direction until equilibrium is reached. Finally, the stabilisation results in a joint equilibrium potential E^e that will be dependent on electrode material, choice of electrolyte and temperature and that serves as an energy barrier to each of the reactions [18].

What is even more relevant for cells and batteries is the current through the cell when an external voltage is applied, bringing the cell out of equilibrium. The voltage applied would change the energy barriers at the electrode meaning either oxidation or reduction would be favoured over the other. For example, a positive applied voltage to cathode, would raise the Gibbs free energy barrier at the cathode meaning it is energetically more favourable for the system to oxidise $\mathrm{LiNi_{0.5}Mn_{1.5}O_4}$ than to reduce Li, leading to a positive net current away from the electrode. A negative applied voltage would naturally favour the opposite reaction and a net current to the electrode [18].

The Butler-Volmer equation describes the relationship between the currents and the applied voltage. It can be derived by applying the law off mass action, where the rate of a reaction is proportional to the activities of the reactants. Assuming that the reaction rate constants are exponentially proportional to the applied voltage:

$$i_{\text{red}} = i^0_{\text{red}} \exp\left(\frac{-\alpha F \eta}{RT}\right) \tag{2.6}$$

$$i_{\text{ox}} = -i^0_{\text{ox}} \exp\left(\frac{(1-\alpha) F \eta}{RT}\right) \tag{2.7}$$

The i_{red} and i_{ox} are the currents stemming from the reduction and oxidation reactions respectively. The voltage η is equal to the difference between the applied voltage and the equilibrium potential $E - E^e$ and is called the *overvoltage*. When the applied voltage is equal to the equilibrium potential, $\eta = 0$ and the currents will be given by i^0_{red} and i^0_{ox}, and since the net current $i_{\text{red}} + i_{\text{ox}}$ should be zero at equilibrium, they must be equal [17]. Finally, the transfer coefficient α is a measure of how large part of the electrode potential will drive the reduction process and tell if one of the reaction directions is hindered more than the other due to obstacles in the cell [18].

The currents according to the Butler-Volmer equation can be seen in Fig. 2.1. As previously mentioned, at $\eta = 0$ the net current is zero and the system is in equilibrium as described by the Nernst equation. For small overvoltages the net current will increase linearly with increased voltage, and the cell will show Ohmic behaviour with a fixed resistance across the interface. For higher voltages the behaviour turns exponential which is also called Tafel behaviour [18].

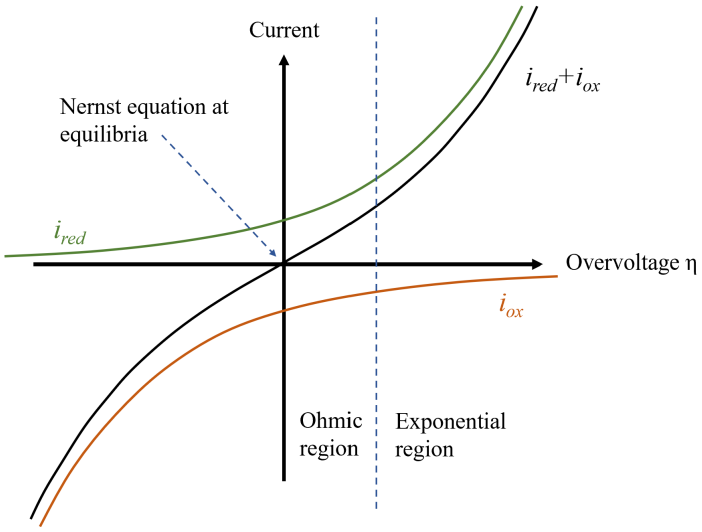

Figure 2.1: The oxidation and reduction current at an electrode/electrolyte interface as a function of the overvoltage in accordance with the Butler-Volmer equation. The net current is seen passing through the origin in accordance with the Nernst equation.

2.2 Mass transport and polarisation

To ensure fast reaction rates and good battery performance, the transport of charged species to and from the electrodes and reaction sites needs to be efficient. Since the movement of ions is slower than for electrons, mobility of ions is of particular importance [19]. There are multiple mechanisms for mass transport through the electrolyte: convection, electric migration due to a potential gradient, and diffusion due to a concentration gradient. For lithium-ion cells the latter two mechanisms are the most relevant [17][19].

The mobility of ions is decisive in how fast the cell can be charged and discharged. The redox reactions are fast, and if ions cannot be supplied to, or removed from, the interface fast enough, there will eventually be an accumulation of positively charged ions on the oxidising side of the cell and a lack of ions on the reducing side. This will create a polarisation in the cell that could hinder the mobility of ions [17]. The flux caused by the diffusion of ions is described by Fick's first law of diffusion,

$$q = D\frac{\delta C}{\delta x} \tag{2.8}$$

where D is the diffusion constant and $\delta C/\delta x$ is the concentration gradient. Since current is charge over time per unit surface and the change in concentration over a small distance can be approximate to be linear, the current just before the interface can be approximated by,

$$i = nF\frac{DA\,(C_B - C_E)}{\Delta} \tag{2.9}$$

Here, A is the surface area of the electrode exposed to the electrolyte, C_B and C_E the concentration of lithium ions in the bulk and at the electrode respectively and Δ the width of the layer where a gradient in concentration exists [17]. This expression gives the current supplied to the reaction sites at the electrode until the concentration at the electrode goes to zero and no redox reactions can occur. Naturally, to increase the supplied current without causing a destructive polarisation, the diffusion constant needs to be high. Approximating the ions as spherical particles with radius r, the Stokes-Einstein equation gives the inverse relationship between the diffusion coefficient and the viscosity μ:

$$D = \frac{k_B T}{6\pi\mu r} \tag{2.10}$$

This means low viscosity liquids are more suitable as solvents in electrolytes [20][21].

2.3 Formation of solid electrolyte interphases

When batteries containing alkali metals, such as lithium, were first cycled together with non-aqueous electrolytes, a thin layer was discovered to appear on the anode surface. The layer, which covered the exposed surface, consisted of decomposed electrolyte. Furthermore, the layer prevented further decomposition of the anode, in the same way rust protects metal, while still letting through lithium ions. The

passivating surface was named the *solid electrolyte interphase* (SEI) and was deemed to have a large influence on the performance during cycling [22]. In 1979 a model for the formation of the SEI and the kinetics of the interphase was proposed that further improved the simpler Butler-Volmer equation [23].

LIBs are high voltage cells that use low potential anodes, such as graphite. The SEI layer is a key element in the development of LIBs, since without it the cell would be unstable, and the decomposition of material would eventually lead to cell breakdown. The SEI extends the stability window of the electrolyte, making cycling with graphite and other alkali metals such as pure lithium as anode possible [24]. Similar passivation layer formation can also be found to occur on the cathode side, called the *cathode electrolyte interphase* (CEI). The CEI also aids in protecting the cathode and electrolyte from decomposition but has not been discussed or researched to the same extent as SEI [25]. However, alongside finding electrolytes with a larger ESW to accommodate high-voltage electrodes such as LNMO, another strategy, while not discussed in this thesis, is to improve the CEI on the cathodes. A more compact and passivating layer on the LNMO surface, while still being permeable to lithium ions, could also ensure the stability of the cell [10].

The composition of the SEI and its microstructure, and therefore its properties, is dependent on the type of electrolyte and electrode used. Additionally, the reduction of the lithium salt and the solvent occurs separately and gives different products. The anion of the salt reduces and forms inorganic products, without carbon and hydrogen bonds, that stick to the anode surface. Meanwhile, the solvent which is often composed of carbonates or other organic compounds, form polymers or semi-carbonates [26]. The conduction of lithium ions through the SEI is due to the properties of the organic components, while the non-reactive properties of the inorganic compounds help protect the surface from further decomposition [22]. Since the formation of the SEI demands the consumption of lithium ions that will subsequently not be able to take part in the intercalation process, there will be an inevitable loss of capacity during the first cycles of the battery. This *irreversible loss of capacity* (IRC) cannot be prevented fully, but efforts are being made to minimise it while still allow the formation of a protective SEI layer [5].

2.4 Electrode materials

The critical properties of electrode materials include their ability to efficiently host and intercalate/de-intercalate lithium into its structure. Furthermore, they should be good electrical conductors with little internal resistance. Preferably, they should also be able to hold as much charge as possible per unit weight and volume. In lithium-ion cells, transition metal oxides with the property to host lithium atoms as interstitials have been used as cathode active material, while variants of carbon such as graphite or hard carbon have been used in the anode. While other electrode materials are consistently being researched and developed, the beforementioned materials have been dominating both the commercial market and research topics [27][28].

The transition metal oxides can be divided into groups according to their structure as well as in which directions the lithium can be intercalated. The layered structure oxides can hold lithium in between atomic layers meaning the lithium can diffuse

freely in two dimensions. Spinel structures (such as LNMO) and olivine structures instead host the lithium in interstitial sites forming tunnels with the former allowing lithium movement in two directions and the latter in only one direction [5][27].

For the electrolyte to be in contact with the largest surface area possible and therefore allow for quick diffusion of ions to reaction sites, the microstructure of the electrode is porous [17]. There are multiple ways to prepare electrodes but usually it involves sputtering, spreading, or spraying of small particles of active material onto a current collector foil, leaving a thin layer of material fully stuck. The particles are mixed with a binder that helps form the film and stick the particles to the electrode. The electrode can also be flattened between heated cylinders to increase the volumetric energy density and improve the contact between its constituents [29]. In high-voltage electrodes sometimes a thin carbon coating is added prior to the active material to prevent corrosion of the collector. From the foil, which usually has a thickness of 10 to 100 μm, electrodes can be stamped out into wanted shape and size.

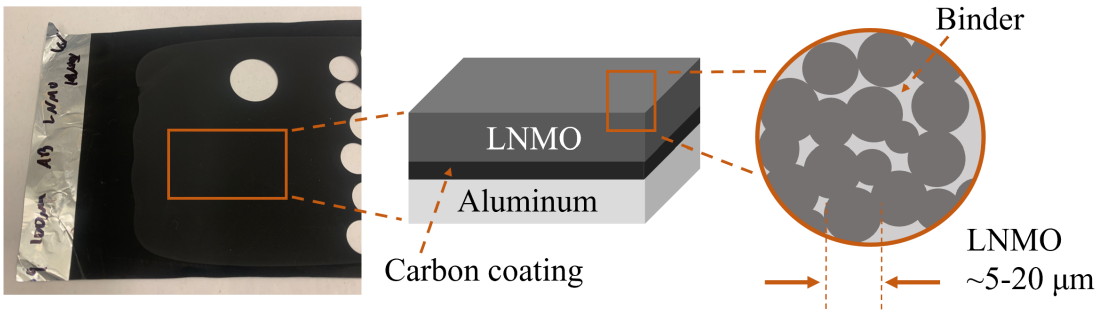

Figure 2.2: Layout and microstructure of an LNMO electrode. The LNMO active material has been applied to a carbon coated aluminium current collector. By adding a carbon coating between the LNMO and aluminium, adhesion is improved and corrosion of the foil may be prevented.

It is the material properties and quantity of the electrode materials used in cells that dictate the theoretical capacity of a full battery. The capacity is measured in either ampere-hours (Ah) or coulombs (C) and is dependent on the maximum number of electrons that can be exchanged in the redox reactions at the interface. By considering the molecular weight M of the active material, the material of the electrode crucial for the reactions, and the quantity of it in the cell, a specific theoretical capacity for the electrode can be calculated,

$$C = \frac{nF}{M}\,\mathrm{C/g} = \frac{nF}{M}\frac{1000}{3600}\,\mathrm{mAh/g} \tag{2.11}$$

In the case of lithium, only one electron is exchanged in the redox reactions, resulting in $n = 1$ [30]. The theoretical values are, as is usual in real life applications, not often reached. The intercalation of ions could for example cause structural instability in the electrode and a passivating SEI could hinder reactions, both resulting in loss of capacity [27]. In Table 2.1 the theoretical (C_T) and practical (C_P) specific capacities of a few common anode and cathode active materials are presented.

2.4.1 High voltage LNMO electrodes

Compared to commercially available cathode active materials, such as LCO and NMC, LNMO has a higher operating voltage of 4.7 V vs. Li/Li+, making it a promising cathode for applications where a high power output is desired. This has been attributed to the reduction and oxidation of the Ni^{2+}/Ni^{4+} pair (by Ni^{2+}/Ni^{3+} and Ni^{3+}/Ni^{4+}) at 4.7 V [27]. Despite it having a slightly lower theoretical capacity than other commercial electrodes, it has been shown to have a better thermal stability than other cathodes and due to its lack of cobalt it is also a relatively cheap and environmentally friendly material [31][32]. Additionally, LNMO has a spinel structure with interstitial sites forming tunnels in the crystal structure, hosting the reduced lithium atoms.

LNMO has not yet been commercially implemented due to its cycling issues. In addition to the lack of electrolytes covering the ESW, LNMO cells with graphite as an anode have shown a gradual loss of capacity after several cycles. The capacity loss implies either a loss of lithium ions participating in the reactions or some sort of deterioration of the SEI or electrode. The cause is believed to be the release of manganese ions into the electrolyte that then diffuse into the bulk and deposit on the opposite graphite. This further encourages the decomposition of other species at the interface, creating a thick impenetrable SEI that also consumes the active Li^+. Consequently, LNMO has also been cycled with lithium titanate (LTO) with better results, since the same deposition of the transition metal ions does not occur. However, since the voltage of LTO against lithium is 1.55 V compared to the 0.1 V of graphite, it means the advantage of LNMO as a high voltage electrode is lost [31][33].

2.4.2 Graphite anodes

Graphite has been the preferred anode in commercial batteries since the end of the 1980s due to its high specific capacity and thermal stability. Before graphite, hard carbon or coke, two types of carbon with a more compact structure, were also used. However, due to graphite having a flatter discharge curve and higher specific capacity, the voltage output was more stable than the other options, leading to graphite taking over the market [5][28]. Like the cathode materials, the graphite is organised in smaller, 10-20 μm particles which are usually deposited on a copper collector. Due to the tendency of lithium to corrode aluminium and form alloys on its surface at low potentials, aluminium current collectors are rarely used on the anode. The size of the particles, impurities in the graphite, and if a protective coating has been applied to the particles are all properties that change between producers and will naturally have a significant effect on the performance of the anode [5].

The intercalation of lithium into the graphite layers is only possible if the layers are correctly aligned. Furthermore, the intercalation will not be homogenous, but the lithium will form clusters in the layers. Depending on the fraction of misaligned layers in the particles, the specific capacity of the anode will be diminished. Furthermore, the intercalation of lithium will cause the expansion of layers, resulting in a volume increase of about 10% from fully discharged to charged [4]. This makes the expansion of the anode an important parameter in the construction of a full-scale

battery and the metal casings which hold the cell.

Table 2.1: Data for a few active materials used in LIBs.

Name	**Structure**	**Formula**	C_T **(mAh/g)**	C_P **(mAh/g)**	**Voltage vs.** Li/Li^+ **(V)**
Cathodes					
LCO	Layered	$LiCO_2$	274 [5]	155-185 [5]	3.9 [5]
NMC622	Layered	$LiNi_{0.6}Mn_{0.2}Co_{0.2}O_2$	275 [34]	140-190 [5]	3.8 [5]
LMO	Spinel	$LiMn_2O_2$	148 [25]	120 [5]	4.05 [5]
LFP	Olivine	$LiFePO_4$	170 [35]	120-160 [8] [36]	3.45 [5]
LNMO	Spinel	$LiNi_{0.5}Mn_{1.5}O_4$	147 [25]	134 [31], 110 [32]	4.7 [11]
Anodes					
Graphite	Layered	LiC_6	372 [25]	355 [36]	0.1 [5]
LTO	Spinel	$Li_{3/4}Ti_{5/3}O_4$	170 [5]	160 [5]	1.55 [5]
Lithium	BCC	Li	3860 [37]	-	0

2.4.3 Lithium metal half-cell configuration

Historically, lithium metal has also been used as an anode although not at the same industrial scale as for graphite and alloys. Lithium metal does not intercalate the ions but instead plates the lithium on its surface during charging and strips the lithium during discharge. The volume increase after charging is higher than for graphite, which may cause issues, but lithium also has a significantly larger theoretical capacity [5][38]. However, lithium metal anodes have not been implemented commercially with liquid electrolytes due to the issue of dendrite formation. The lithium is not plated uniformly on the surface of the lithium metal anode but can during multiple cycles instead form spiky structures that poke into the electrolyte. If the dendrites reach the cathode, the cell will be short circuited which constitutes a severe safety hazard in applications [38].

In research however, lithium anodes have found another purpose and are commonly used as a standard electrode against both anode and cathode materials to isolate the performance of only one electrode. Lithium is a stable reference potential, and its high capacity also ensures that it does not set the capacity limit of the cell setup. This setup is often called a half-cell as it only focuses on the behaviour and characteristics of one of the electrodes and the electrolyte [39]. Since the cells in research often are not cycled as many times as full batteries and are not as sensitive to short circuiting, the lithium metal anode is often utilised and is an important tool in the characterisation of electrochemical cells.

2.5 Electrolytes for LIBs

The role of the electrolyte in an electrochemical cell is to separate positive and negative charge and to transport the positive ions between electrodes during charge and discharge. Furthermore, it must do this reliably for many cycles. A high ionic conductivity, low electronic conductivity and good electrochemical stability are therefore the key properties of a functioning electrolyte. The source of lithium ions in the LIB electrolyte comes from the solvation of lithium metal salts in some type of solvent. This also requires the electrolyte to have good salt solubility properties to solve enough salt for the operation of the cell and not form precipitates [7]. This can be measured in permittivity, as a solvent with a high dielectric constant will solve ionic compounds more easily. In Section 2.2, it was shown that low viscosity materials facilitate the movement of ions through the electrolyte. Unfortunately for many commercial electrolytes, this property rarely goes hand in hand with a high dielectric constant. As a consequence, they are almost exclusively mixtures between solvents of varying properties [18]. Furthermore, the electrolyte needs to be able to form a thin but protective layer of SEI together with the electrode to allow the permeation of ions but simultaneously protect against degradation [7].

The benchmark electrolyte used in LIB applications is lithium hexafluorophosphate, $LiPF_6$, in a mixture of carbonate esters such as ethylene carbonate (EC), dimethyl carbonate (DMC) or diethyl carbonate (DEC). This class of electrolytes is the one used almost exclusively in commercial applications and has been shown to form a good SEI while being stable in the ESW set by commercial anodes such as LCO or LFP [7][16]. EC has a high dielectric constant but is a solid at room temperature, while DMC and DEC are of low viscosity with high ionic mobility [18]. Beyond these electrolytes, there is a vast number of solvents and salts all with greatly varying properties. In addition to organic solvents, ionic liquids (IL), salts that are liquid below 100°C, have become popular both as solvents as well as additives due to their large ESW as well as their thermal stability [10]. The tuning of salt concentration and composition creates a near infinite selection of electrolytes. In this section some of the most common salts, solvents, and ionic liquids, as well as ones relevant for the scope of this thesis, are presented.

2.5.1 Lithium salts

The most important properties of the lithium salt are dissociation degree, solubility in the solvent, and both chemical and thermal stability. Additionally, together with the solvent, it should help form a good SEI. In almost all commercial applications, lithium hexafluorophosphate ($LiPF_6$) is the salt used due to its high ionic conductivity and its compatibility with graphite anodes [7]. The anion is constituted by a central phosphorous atom, bound to six surrounding fluoride atoms in an octahedron shape. The P-F bonds are, however, relatively weak and in the presence of water and high temperatures, the anion can undergo hydrolysis creating highly toxic hydrogen fluoride gas. In the case of battery malfunctions where water could penetrate the cell this is a concern, especially in the case of high voltage electrodes and in electric vehicles where the temperatures are heightened [18].

Other salts, known for their superior thermal stability as well as their stability against hydrolysis, are lithium bis(fluorosulfonyl)imide ($Li[N(SO_2F)_2]$) and lithium bis(trifluoromethanesulfonyl)imide ($Li[N(SO_2CF_3)_2]$), more commonly known as LiFSI and LiTFSI, respectively. Since the S-F bond in FSI is weaker than the C-F bond in TFSI, the latter anion has a slightly higher thermal and electrochemical stability. However, electrolytes of both show slightly lower ionic conductivities than when using $LiPF_6$ [7][40]. Also, important to mention is the tendency of LiTFSI and LiFSI to corrode the aluminium foil current collector at the cathode. Curiously enough, an exception to this is ionic liquids with TFSI or electrolytes with a high concentration of the salt [7].

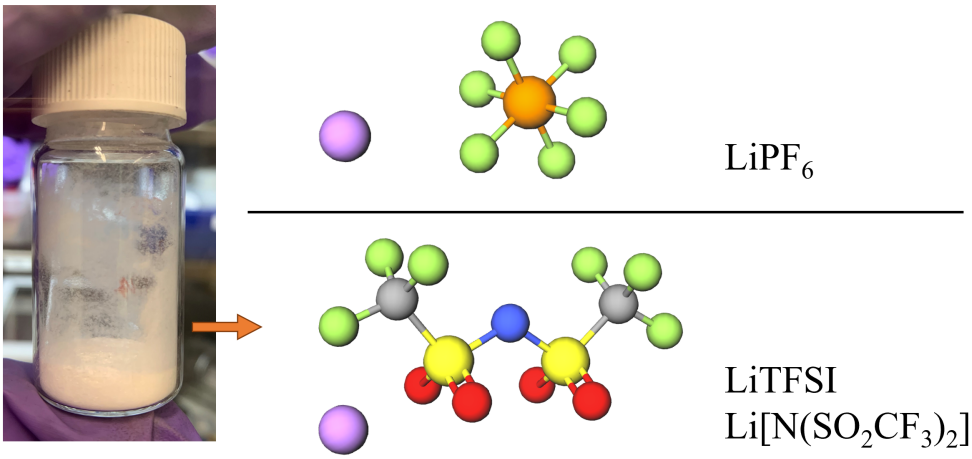

Figure 2.3: The chemical structures of two common lithium salts. LiTFSI is a solid crystalline powder at room temperature. Since the P-F bond of the $LiPF_6$ is less stable than the C-F bonds, LiTFSI is more suitable for cells with a high voltage cathode. Models made with MolView.

Another area of research is high concentration or solvent-in-salt electrolytes where the salt concentration is raised from the conventional 1-2 M (mol/dm^3) to up to 1:1 molar ratio. Since the ratio of salt is so high, there are few available free solvent molecules. The ESWs are wide, and the electrolyte becomes less volatile. The downsides of these types of electrolytes are their high viscosities, reducing the ionic mobility. Additionally, the high viscosity can cause slow or bad wetting of separators and electrodes, leading to poor contact and slow reactions in the battery [10][41]. Finally, in addition to the already mentioned, there is a plethora of salts being researched and developed. Furthermore, adding a level of complexity is the mixing of two or more salts to fine-tune the desired properties [42].

2.5.2 Non-aqueous organic solvents

Organic solvents are the most common medium for the dissolution of lithium salts in liquid electrolytes. Aqueous LIBs with water as a solvent also exist, with for example spinel oxides as cathodes, although with different anode materials. However, due to the narrow ESW of the aqueous electrolytes of about 1.23 V, they are effectively

eliminated from being used in an oxide/graphite cell [43][44]. Instead, carbonate esters, ethers and other organic compounds are the basic solvents found in LIBs. A common property for most of the organic solvents is their flammability, which has been and still is a challenge in LIB research, although a selection of additives to the solvents has been shown to significantly improve battery safety [42].

As previously mentioned in the benchmark example at the beginning of section 2.5, the carbonate esters are the most established solvents due to their low viscosity, good ionic conductivity and high dielectric constant, as well as their sufficient electrochemical stability with commercial electrodes [10][38]. The carbonate esters can be divided into linear carbonates (DEC, DMC, EMC) and cyclic carbonates (EC, PC) depending on the chemical structure, which also gives them different properties. DEC has linear chains which lowers the viscosity compared to the ring-shaped EC, which instead has a higher dielectric constant [38]. The carbonate esters also form a very stable SEI making them suitable against graphite anodes. The downside of the carbonates however is the limited ESW in the case of high voltage electrodes.

Ethers have not been utilised to the same extent as carbonates as they have shown to not be stable against cathodes operating higher than 4 V. However, in a dual electrolyte setup the ether could potentially work against the anode side. Moreover, they are less flammable than the carbonates making them relevant as an additive [44]. The most common ether in connection to LIBs is dimethoxyethane (DME), also known as glyme which has been paired together with PC and EC to lower the viscosity and create non-flammable electrolytes [45][46].

To improve the properties of both carbonate and ether solvents, fluorine atoms can be added to the compounds. It has been proved to both increase the stability range as well as making the solvent less flammable [7][10]. One example is the addition of fluoride to EC, resulting in fluoroethylene carbonate (FEC), that has been shown to form a superior SEI on both anode and cathode in high voltage systems [5][36]. Furthermore, organic compounds containing sulphur such as dimethyl sulfoxide (DMSO) and sulfolane (TMS) have also been utilised as solvents due to their low flammability and high dielectric constant. In comparison to ethers, they are more stable against various cathodes but have issues forming proper SEIs due to their high viscosity [38].

Table 2.2: Viscosity and ionic conductivity of some organic solvents at room temperature (293 K).

Solvent	**Type**	**Viscosity (mPa·s)**	**Ionic conductivity, (mS/cm), 1 M $LiPF_6$**
EC	Cyclic carbonate ester	1.9 (40°C) [7]	6.9 [5]
PC	Cyclic carbonate ester	2.5 [7]	5.2 [5]
DMC	Linear carbonate ester	0.59 [7]	6.5 [5]
DEE	Ether	0.288 [47]	-
DBE	Ether	0.414 [48]	-
DMSO	Organosulfur compound	1.99 [7]	∼11 [49]
TMS	Organosulfur compound	10.28 [7]	0.2 (in 1 M LiTFSI) [50]
FEC	Fluorinated ether	∼4 [7]	5 [7]

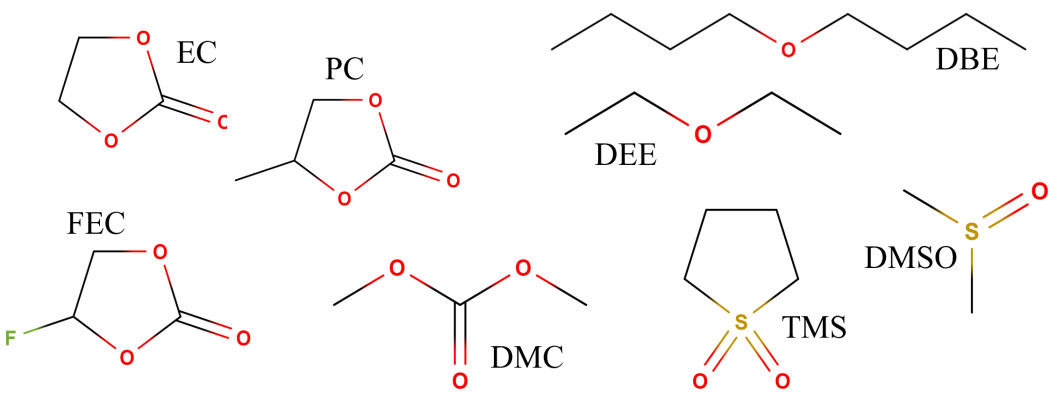

Figure 2.4: Chemical structures of some organic solvents. Models made with MolView.

2.5.3 Ionic liquids

Ionic liquids (ILs), salts that are liquid below 100°C, and most often are also room-temperature ILs, were first brought to the attention of LIB researchers when new cation-anion pairs were developed which were water-insensitive and resistant to hydrolysis. The ILs have for some time been considered promising due to their high thermal stability as well as their expanded ESW compared to organic solvents [50]. At high temperatures their ionic conductivity is relatively high, but they often show high viscosity at room temperature, potentially limiting diffusion of lithium ions. Additionally, due to the large selection of both anions and cations and the various pair they form, ILs can be considered "designer solvents" where there is a large spread of properties available. The desired properties of ionic liquids are the same as for organic solvents, namely good salt solubility and good SEI formation and they are simultaneously being researched as a stand-alone solvent and as an additive. Issues with ILs include their viscosity, leading to bad wetting of the separator and electrode, as well as problems with forming SEIs and CEIs against various electrodes that cycle well [7][45][51].

2.5.3.1 Cations

Generally, the positively charged cations of ILs are organic compounds in either ring formations such as the pyrrolidinium (PYR) and imidazolium (Im) or an inorganic atom such as phosphorous, aluminium or sulphur with chains of organic groups, such as alkyls, attached [51]. The imidazolium ILs were the first to be researched and showed better ionic conductivity than organic solvents. The Im-cations include two highly reactive acidic hydrogen groups, lowering the upper cathodic limit of the ESW of ILs with the cation [10]. Furthermore, on low voltage anodes such as graphite, ILs with Im-cations would reduce and not form a proper SEI, although adding small amounts of carbonate solvents was shown to help with the formation [38]. PYR-based ILs exhibit higher cathodic stability than Im, even up to 5.5 V against lithium for some anions, while simultaneously having lower viscosity. Like most ILs,

it forms an improved SEI with the addition of organic solvents and therefore has a better anodic stability, but with the drawback of a reduced ESW [51]. ILs based on aluminium and phosphonium atoms have been researched less due to their high melting temperature and high viscosity. However, they have shown to be stable against several cathode materials as well as pure lithium anodes [52].

2.5.3.2 Anions

The anions of ILs relevant for LIBs are primarily the same anions as for the lithium salts, such as $[PF_6]^-$, $[BF_4]^-$, $[TFSI]^-$ and $[FSI]^-$. Moreover, it is believed that the anion is the determining factor when it comes to anodic stability [38]. A larger anion causes the ionic bond between anion and cation to be weaker, meaning they dissociate ions better leading to better mobility. For example, $[FSI]^-$ has showed better ionic conductivity and lower viscosity than $[TFSI]^-$ due to the molecule's smaller radius [52].

Table 2.3: Some properties of a selection of ionic liquids.

Trivial name	**Cation/ Anion**	**ESW (V)**	**Viscosity (mPa/s)**
PYR14TFSI	1-butyl-1-methylpyrrolidinium/TFSI	5.88 [53]	84.33 [54]
EmimTFSI	1-ethyl-3-methylimidazolium/TFSI	5.5 [55]	35.55 [56]
P_{66614}TFSI	trihexyltetradecylphosphonium/TFSI	-	304 [57]
$BmimBF_4$	1-butyl-3-methylimidazolium/BF_4^-	5.3 [58]	72.51 [59]

2.6 Separators

Without an insulating separator between electrodes, the cell runs the risk of short circuiting. Since the separator must allow ion permeation, the separators are made porous in order to soak up the electrolyte. This presumes that the electrolyte is able to wet the material. Additionally, the materials need to be durable and stable when put under elevated temperatures and charge [5]. Traditionally, materials such as glass fibre and polymers have been used. An example is Celgard, a membrane made from polypropylene and polyethylene which is often used in battery research. The thickness of these separators is typically 10-25 μm with a pore size of less than 1 μm. In the case of a dual electrolyte setup, the capillary forces of the separators when soaked with different electrolytes are crucial in preventing mixing of the electrolyte. A system where the electrolytes completely wet their separators and the separators are compressed minimally after wetting would be ideal. Furthermore, there should be good contact between electrolytes, and preferably the capillary forces should contain the electrolytes fully.

2.7 Research cell configurations

Naturally, there is no point in building a full-size commercial battery when testing new materials for LIB applications, as it is neither economical nor resourceful. Instead, smaller setups are used to characterise the cells, designed after the intended characterisation method. To evaluate the performance of the batteries, the batteries are cycled by varying the applied current or voltage across the cell while measuring and recording the resulting voltage, current or impedance. To further understand the mechanisms of the cell, other characterisation techniques such as optical spectroscopy or tomography can be used to study the materials during cycling. In these cases, special cells that expose the area of interest can be constructed, an example being the *in situ* Raman spectroscopy cell used in this work, which will be detailed further on.

To avoid contamination and oxidation of the cell and prevent moisture in non-aqueous electrolytes, the cells are assembled in an inert environment, most often in an argon-filled glovebox. While some gloveboxes allow cycling of batteries inside, the cell materials are most often placed in a container that can be closed off and sealed off from air and moisture and then taken out of the glovebox to be cycled. Finally, important to note is while these cells are intended to emulate the performance of industrial battery stacks on a smaller scale, there will always be limitations. Examples include differences in electrolyte and active material ratios, heat generation and dissipation as well as available surfaces for reactions [60]. Nevertheless, they are important tools in research and in the development of new materials.

2.7.1 Coin cells

The most common and simple cell used for electrochemical characterisation is the coin cell, a small flat cylindrical cell which is available in multiple sizes and dimensions. The standardised CR2032 coin cell is often used and has a diameter of 20 mm and height of 3.2 mm when assembled. Fig. 2.5 shows the components of a conventional coin cell stack before assembly. One electrode is placed in the case with the current collector side of the electrode towards the metal, while the other electrode will be in contact with the spacer. The role of the spacer and spring is to assert pressure on the stack to ensure good connectivity between the parts of the battery. Different thickness of spacer can be used to better control the pressure inside the cell.

The gasket is a plastic ring which prevents the cell from short circuiting by separating the case and cap and also makes the cell airtight. Likewise, the separator is cut slightly bigger than the electrodes to avoid accidental contact between them. The contents and metal casing of the cell are simply stacked and are thereafter placed in a closing device which crimps the edges, sealing the cell from the environment. When cycled, the two poles are connected to the flat top and bottom. After cycling, the cell can be opened by bending the case open, but not without some disturbance of the cell stack.

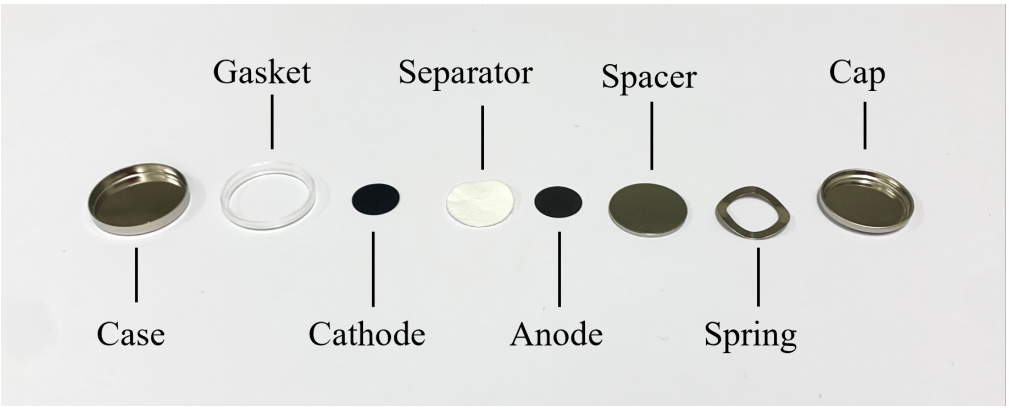

Figure 2.5: Components of a coin cell battery. The cathode and anode are attached to the metal current collectors as previously described in Fig. 2.2.

2.7.2 Swagelok cells

Another configuration, more easily taken apart, is the Swagelok cell. The electrodes and separator are placed in a hollow tube made of fluorinated polymer and compressed by two metal cylinders on each side. Next, a plastic casing is screwed on the tube, with packings ensuring isolation from the environment. Furthermore, pistons inside the tube makes it possible to control the pressure asserted on the cell stack. The cylinders are in contact with the electrodes and by inserting pins in the holes at the ends of the cylinders, the cell stack can be connected to an external circuit.

The result is a cell that is easily assembled and disassembled, making it possible to remove the electrodes and separator for further characterisation such as spectroscopy or microscopy. Another advantage of the Swagelok is the possibility to cycle the cell at higher temperatures. The plastic gasket of the coin cell is at risk of deforming which may cause the cell to leak while the fluorinated polymer casing is less sensitive to heat.

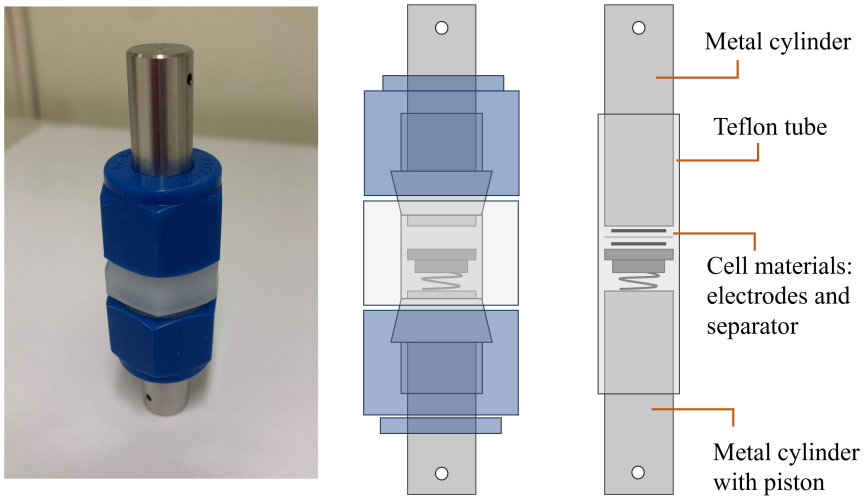

Figure 2.6: The Swagelok cell and its inner components.

3

Immiscibility and diffusion of electrolytes

To realise a dual electrolyte concept based on the immiscibility of electrolytes, the first natural step is to find appropriate liquids that in theory fulfil the requirements of a LIB electrolyte. This chapter presents the results of a literature review where electrolyte pairs have been found and subsequentely tested for their immiscibility. The compatibility of the electrolytes with common separators were also investigated since proper wetting is crucial to prevent diffusion between the pairs.

Multiple techniques were considered to study the diffusion in the separators. Since the most crucial component of the dual electrolyte concept is to prevent the contact between one electrode-catered electrolyte and the other electrode, diffusion close to the electrolyte/electrolyte interface was deemed not to be the primary issue at this stage. Instead, the question asked was if the emulsion region of mixed electrolytes was thin enough to ensure that the electrolytes did not seep through to the opposite electrode. Furthermore, as the assembly of a cell stack involve applying pressure to guarantee good contact, this element should also be included. Optical spectroscopy techniques to detect the presence of electrolyte on the separators were deemed to be the best approach, due to the possibility of distinguishing between molecular species and their non-destructive nature, ensuring that the probing of the material would not interfere with the diffusion or cause mixing. Additionally, a number of spectroscopy instruments were readily available at the Material Physics division at Chalmers.

A first attempt at characterisation of the separator surface was made using a Swagelok cell and attenuated total reflectance Fourier-transform infrared spectroscopy (ATR-FTIR). Two separately wetted separators containing the electrolytes were placed in the cell together, compressed and left for 24 hours, replicating the assembly and environment of a real cell but without electrodes. ATR-FTIR is a technique where infrared laser light is directed onto either a solid or liquid sample placed on a crystal, making fast identifications of materials at a depth of 1-5 μm by analysing the reflected spectra. Another advantage of using the ATR-FTIR spectrometer was its placement inside the glovebox, making measurements possible without having to remove the cell and the separators from the inert environment. After resting, the cell was disassembled and both sides of each separator were measured to check for the presence of the opposing electrolyte. However, the measurements of solid materials involved pressing the separator against the crystal with a clamp to get a good signal, which probably interfered with the diffusion. Moreover, it was also difficult to assess how the removal of the separators from the Swagelok tube

affected the measurements, making the results unreliable.

A more uninvasive technique was developed after taking inspiration from Raman spectroscopy *in situ* measurements of graphite electrodes. A special cell, developed specifically for Raman measurements, was used to make measurements of one side of the separator without removing it from the other. The cell also provided an isolating environment, preventing evaporation and contamination, as well as offering the possibility to assert pressure on the separator stack without opening the cell. This chapter presents the theory behind Raman spectroscopy, a technique that like ATR-FTIR can identify the presence of species on the surface of materials by analysing the chemical structure. It is followed by a discussion on the penetration depths of transparent or semi-transparent materials, like the glass fibre or Celgard separators and their significance on the measurements. Finally, the chapter concludes with the results of diffusion measurements of two of the pairs, one IL/IL and one solvent/IL.

3.1 Immiscible electrolytes

The concept of immiscible electrolytes that can carry charges across their interface is not new. For instance, the interface between two immiscible electrolyte solutions (ITIES) has for example been used since the early 1900s as a physical model to study the characteristics of biological membranes that also transfer charged particles across an interface [53]. Other practical applications include sensors for electrochemistry measurements and in pharmaceutical studies in connection to the delivery of drugs [61]. Although not discussed in detail in this thesis, which mainly focuses on the diffusion, the charge transfer across the interface is significant for the ionic mobility and therefore also for the operation of the cell.

3.1.1 Polarity of solvents

Liquids that fully mix do so because the total internal energy for the mixture is lower than that of the liquids separately. It is thermodynamically favourable to break the interactions between the same molecular species and form new in the mixture. Liquids with similar interaction strength and polarity are more likely to mix and form a miscible solution than pairs for which it differs, a simple example being organic chains like hexane not mixing with water, a high polarity molecule. In this work, this was taken as a rule of thumb when searching for solvents, while keeping in mind that other factors may affect solubility. Nevertheless, solvents used in LIBs need also to be able to solve the polar bonds of the lithium salts, meaning low polar solvents such as hexane are excluded, at least as a stand-alone solvent [62]. The targeted solvents were therefore in the rough range of slightly polar to polar.

3.1.2 Immiscible pairs

In the early stages of the review, no solvents or ILs were excluded based on their documented cycling performance in LIB cells, as the main interest lay in the study of diffusion. However, the electrolytes tested for their immiscibility and thereafter selected for the measurements were in part decided by the availability at the Material

Physics laboratory, as the lead time for some chemicals, especially the ILs, did not match the time plan. While a number of immiscible pairs were found, unfortunately no solvents used in commercial electrolytes, such as PC and EC, were found to be immiscible. The carbonate esters were instead found to be miscible with a wide range of solvents only excluding non-polar liquids such as gasoline and turpentine.

Solubility charts from chemical and pharmaceutical company Merck indicated the immiscibility between the polar solvent dimethyl sulfoxide (DMSO) with several non-polar solvents such as diethyl ether (DEE), dimethyl formamide (DMF) and dimethoxyethane (DME). The downside of DMF and DME is their high toxicity ([63][64]) making them less than ideal when handling them in a diffusion study, outside of a glove box. Furthermore, the boiling point of DEE is only 34.6°C making it highly volatile and unsuitable in battery applications. Instead, dibutyl ether (DBE) was considered due to its slightly longer alkyl chains with four alkyl groups on each side of an oxygen atom instead of two. The longer chains result in stronger intermolecular bonds, raising the boiling point to 142°C. In a glovebox, DMSO and DBE were added to a small glass vial, shaken, and left to stabilise with the higher density DMSO on the bottom. The result can be seen in Fig. 3.1, showing a small visible meniscus and proving immiscibility.

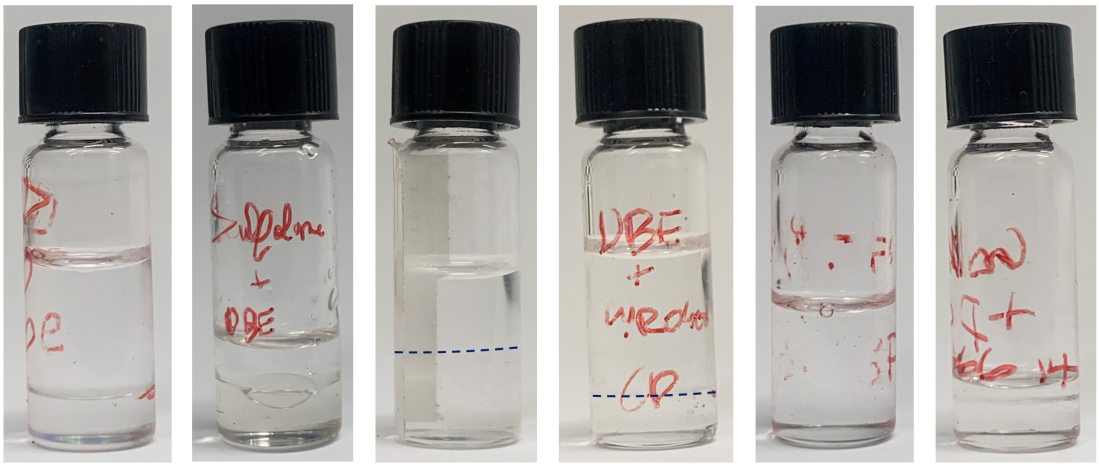

Figure 3.1: Mixed electrolytes. a) DBE and DMSO, b) DBE and Sulfolane, c) DBE and [PYR14][TFSI], d)DBE, [PYR14][TFSI] and TMS, e)[PYR14][TFSI] and [BmimBF$_4$][TFSI], f)[P$_{66614}$][TFSI] and [Emim][TFSI].

Continuing, datasheets from Solvionic, a chemistry company specialising in ILs, stated that several PYR-ILs and Im-ILs were immiscible in DEE and other non-polar solvents such as hexane and toluene. This could be expected given the polarity of the freely moving anions and cations in the IL. The well documented 1-butyl-1-methylpyrrolidinium bis(trifluoromethylsulfonyl)imide, [PYR14][TFSI], was selected, and tested together with DBE, also showing a clear meniscus, although hard to see on the picture. Compared to the organic solvents, [PYR14][TFSI] had a higher viscosity and the two phases, with [PYR14][TFSI] at the bottom, took longer to stabilise after the vial was shaken. One of the articles presenting a dual

electrolyte configuration for a lithium-sulfur battery, by Ren and Mantiram [14], demonstrated the immiscibility between DBE and TMS. The less viscous mixture of [PYR14][TFSI] and TMS in 1:1 volume ratio was mixed with DBE, and also proved to be immiscible.

Moreover, a few IL/IL pairs were also tested. It was reported in literature that imide-based ILs, with anions such as $[TFSI]^-$, were immiscible in water while borate-based ILs like $[BF4]^-$ were not. Therefore two ILs with these anions were tested, paired with two different cations, [PYR14][TFSI] and 1-butyl-3-methylimidazolium tetrafluoroborate [Bmim][BF4]. In this case, the liquids were fully miscible, even after leaving it to stabilise for several weeks. Additionally, it would have been interesting to test these anions with the same cation, but due to [PYR14][BF4] being crystalline at room temperature, this was not done. Finally, a 2006 article by Arce et al. ([65]) documented the immiscibility between the two ILs tetratrihexyltetradecylphosphonium TFSI, $[P_{66614}][TFSI]$, and 1-ethyl-3-methylimidazolium TFSI, [Emim][TFSI]. This pair was therefore also tested, and their immiscibility proved, with [Emim][TFSI] settling on the bottom. Out of the pairs, $[P_{66614}][TFSI]$ and [Emim][TFSI] exhibited the highest viscosities.

3.1.3 Wetting of Celgard and glass fibre separators

Proper wetting of the separators, meaning all porosities in the material are filled with electrolyte, is important for the performance of LIBs since empty space in the cell would mean higher resistance and lower ionic conductivity across the cell. Furthermore, in a dual electrolyte and separator cell the improper wetting of one of the sides could lead to the diffusion of the other electrolyte into the opposite separator, filling up the empty porosities. In this thesis, glass fibre separators made of borosilicate glass and Celgard 2400, made of polypropylene, were used. All solvents in the immiscible pairs mentioned previously, were able to wet the glass fibre separators relatively well which could be seen by the separator turning semi-transparent when filled. However, higher viscosity electrolytes, namely the ILs $[P_{66614}][TFSI]$, [Emim][TFSI] and [PYR14][TFSI] were all slow to fill the glass fibre, taking up to a couple of minutes to properly diffuse into a 10 mm diameter, 260 μm thick separator.

While DBE easily wet Celgard, turning the separator almost entirely transparent, [PYR14][TFSI] first formed a bead on the surface before slowly diffusing into the material. The process could be sped up slightly by wetting the Celgard from the side, where presumably the fibres were aligned differently. $[P_{66614}][TFSI]$ also wet the separator rather slowly but did not form an initial bead. The two remaining electrolytes, DMSO and [Emim][TFSI], would not wet Celgard at all. Separators were placed in vials and completely covered in the electrolytes, but even after being left for weeks, the separators floated to the top of liquid or stuck to the walls of the vials without being wetted at all. This has likely to do with the long organic chains of the polymer and how it differs from the short aromatic ring of $[Emim]^+$ and the short polar molecule of DMSO. In comparison, DBE, $[PYR14]^+$ and $[P_{66614}]^+$ all have slightly longer alkyl chains connected to an oxygen atom, pyrrolidinium group and phosphonium atom respectively. The difference makes it unfavorable to form intermolecular bonds.

However, the non-wettability of some solvents might not be an issue at all since it could be used to further ensure that no diffusion takes place between separators. Using glass fibre for [Emim][TFSI] and Celgard for $[P_{66614}][TFSI]$ would make it theoretically impossible for [Emim][TFSI] to diffuse through the separator. Nonetheless, under enough pressure in the cell the liquids could still escape around the separators to the opposite electrodes. Furthermore, two different separators could potentially hinder the mobility of ions if it creates an isolated interface without an intermediate emulsion layer. In the Raman measurements, both pairings of separators were tested.

3.2 Raman spectroscopy

Raman spectroscopy is a noninvasive spectroscopy method capable of identifying materials by analysing inelastically scattered photons off the sample. The technique probes the vibrational modes of the molecules, revealing information such as chemical structure, molecular orientation, and strength of bonds without damaging the sample. It has since the 1960s been an important characterisation method, that can both probe solids, liquids and, in the right setup, even gases. Furthermore, it is quick while still making it possible to detect specific compounds on a micrometer scale [66]. In this section, the underlying interactions between vibrational energy levels in the molecules, resulting in identifiable spectrums, are explained. Moreover, the Raman spectrometer is introduced together with the Confocal spatial filter and it is explained how the latter makes it possible to achieve even more precise measurements, as well as measurements along the vertical axis.

3.2.1 Theory

A simple model of the energy states of a material can be seen in Fig. 3.2, with E_0 being the ground vibrational state and ν_1 the first vibrational energy state. A monochromatic beam, for instance a laser, is directed onto the sample and a photon is absorbed, leaving the molecule in a virtual energy state. The interaction between the absorbed photon can either be elastic, namely Rayleigh scattering, or inelastic, Stokes and Anti-Stokes. In the case of the former, a photon will be emitted with the same frequency as the absorbed one, leaving the molecule in the initial ground state. If the molecule falls back to a different vibrational state, the emitted photon will experience a change in energy equal to the distance between ground state and the first vibrational state. This is called the Raman shift, and since different molecules have different energy configurations, the photons from the shift can be measured to characterise the material.

If the molecule is already in a higher vibrational state, it can, after absorbing a photon, fall back to the ground state and emit a photon of higher frequency than the absorbed photon. This is called Anti-Stokes scattering which can also be measured, although it is not used as frequently for characterisation as Stokes scattering. The scattered photons are counted as a function of their frequency, creating a spectrum that can be used to identify the molecule. Instead of frequency, the intensity is plotted against the Raman shift, measured in cm^{-1} which is the

difference in wavelength between the energy states. Naturally the peak formed by the Rayleigh scattered photons will be located at 0 cm^{-1} [66]

A challenge when performing spectroscopic measurements is the fluorescence of the material, which is in many cases inevitable. Fluorescence is the result of transitions between electronic energy levels, in contrast to the vibrational levels responsible for the Raman shift. The fluorescence does not form peaks on the spectrum but instead leaves a baseline, as is visible in the spectrum presented in Section 3.4.1. In addition to data processing and background fitting of the fluorescence, changing the wavelength of the laser beam may help reduce fluorescence since photons with longer wavelengths will not have enough energy to excite the photons to a higher electronic energy level [66].

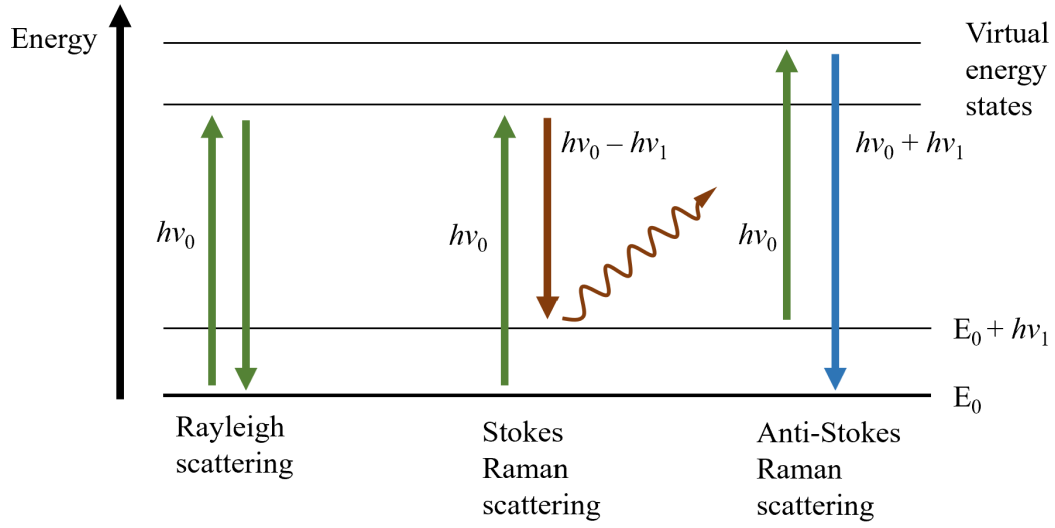

Figure 3.2: Energy states of a molecule absorbing a photon. The scattering can either be elastic (Rayleigh) or inelastic (Stokes and Anti-Stokes) with the latter emitting a photon of a different wavelength

A simplified instrumental setup of a Raman spectrometer can be seen in Fig. 3.3. This instrument is equipped with a confocal filter which gives a better spatial resolution, both vertically and horizontally in the sample. By changing the pinhole of the confocal filter, only scattered light from a specific area will reach the detector, making it possible to perform detailed profiling of the sample along different axes, even into the sample. However, less light will be let through to the detector, which will give a weaker signal. In addition to the pinhole, the objective will also affect the resolution since it determines the area of illumination as well as the numerical aperture and the maximum angle at which the reflected light will be collected. A higher magnification on the objective will focus the laser beam in a smaller area, reducing the sampling area and improving the spatial resolution.

Furthermore, inside the spectrometer the scattered photons are spatially dispersed by a diffraction grating and counted when hitting the *charge coupled device* (CCD) detector. Changing the diffraction grating to a higher groove, broadens the dispersion of photons on the detector, which in turn increases the energy resolution

of the spectrum. However, it comes at the cost of longer measurement times, as the entire energy range will not fit on the CCD detector. Instead, multiple measurements will need to be done to cover the full range. The period of time reflected light is allowed through to the detector is called the *acquisition time*. Longer acquisition times will give more counts on the detector and higher intensity but will not necessarily give less noise. Instead, the same acquisition can be performed a number of *accumulations*, which will thereafter be averaged, which may give a cleaner signal.

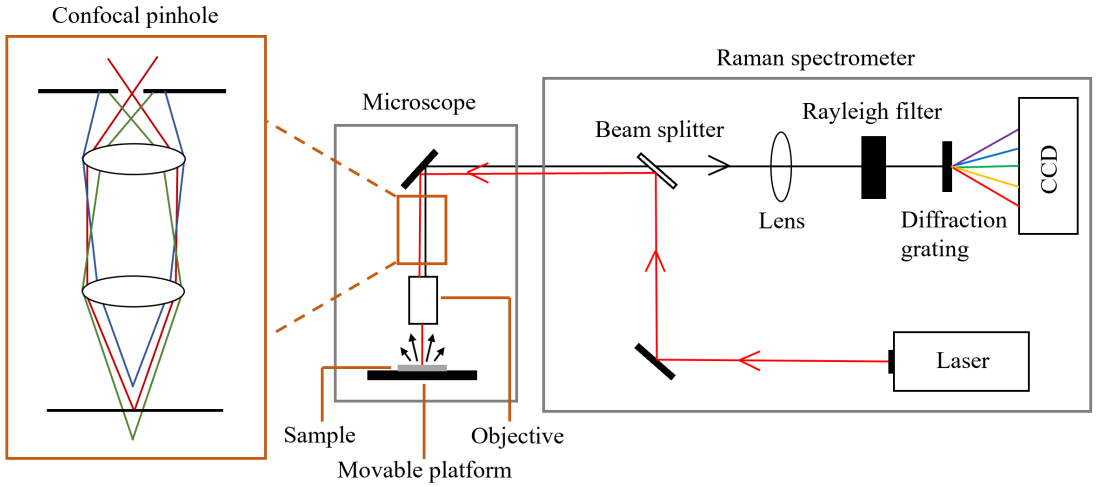

Figure 3.3: A Raman spectroscopy instrumental setup. With a confocal filter, the spatial resolution of the spectrum as only light from the focal plane will be able to pass through the pinhole. Decreasing the size of the pinhole, will increase the resolution at the cost of a weaker signal.

3.2.2 Raman penetration depth in separators

In order to make reliable measurements of the diffusion in the separators, the penetration depth needs to be considered. Since the thickness of the separators is small, and given the separators turn semi-transparent when wet, there is a risk of the penetration depth of the photons being as deep as the separators are thick, resulting in the Raman spectrum covering the entire material. The theoretical maximum depth resolution set only by the objective can be approximated with

$$\Delta z \approx \frac{2\lambda}{(NA)^2}, \tag{3.1}$$

where Δz is the *full width at half maximum* (FWHM) of the point spread function along the optical axis, λ the wavelength of the laser, and NA the numerical aperture of the objective [67][68]. This value will give the maximum probing depth of the laser, meaning that outside of this range the intensity of the reflected light will be weak. Furthermore, the limit of lateral resolution will be determined by the spotsize of the laser on the focal plane given by

$$\Delta x \approx \frac{1.22\lambda}{NA} \tag{3.2}$$

This will give the smallest possible distance two points on the sample can be distinguished from each other. For NA=0.25, the smallest aperture of the objectives used in this work, and lambda=633 nm (red laser), $\Delta z = 20\,\mu$m and $\Delta x = 3\,\mu$m , and for NA=0.5, $\Delta z = 5\,\mu$m and $\Delta x = 1.5\,\mu$m, Given that the thickness of the Celgard and glass fibre used in this work is 25 μm and 260 μm respectively this is an issue, at least for Celgard measurements. Furthermore, this is the theoretical limit. In practice, the material will further diffuse the laser beam, lowering both the lateral and depth resolution, especially in the case of transparent materials.

However, with a confocal spatial filter the depth resolution can be improved and measurements inside transparent samples can be made. By calculating the spread of the reflected light on the back focal plane an intensity ratio between the Raman-scattered light transmitted through the pinhole and the initial light intensity can be calculated. The point spread function will have the shape of a Lorenztian curve centred around the focus point of the laser in the material and the width of the curve will be dependant on the numerical aperture, pinhole diameter and the magnification of the objective. A geometrical model to calculate this function was introduced and verified experimentally by Tabaksblat et. al. [69]. By measuring on a $2\,\mu$m thick polyethylene film on top of a thicker polypropylene film they could measure at which instrumental settings polypropylene showed up on the spectrum. For a objective of 50x and a pinhole of 300 μm, the depth resolution (defined as the FWHM of the point spread function) was deemed to be 3 μm, and 1.5 μm for a 100 μm pinhole which was in line with their model. This is more promising for measurements of the separators.

There are additional effects that should be taken into consideration. Tabaksblat's model does not take into the account the effects of refraction at the sample interface. A high refractive index will shift the focus point of the laser further down in the sample, altering the depth resolution [70]. The measurements by Tabaksblat et. al were on dry polymers, while the separators are porous and will be wetted. This will change the refractive index, but it is unsure by how much. Furthermore, the electrolytes will possibly have slightly varying refractive index depending on their viscosity. Everall ([70]) proposed a correction to the depth resolution taking into account the refractive index, however only for homogenous samples. Finally, FWHM approximation of the point spread function is somewhat simplified. While the majority of the signal will come from within this depth profile range, it still as a tail that could interfere with measurements. Interactions with the sample outside of the range might very well show up on the spectrum, especially if the material is more prone to Raman interactions than the material at the focus point.

3.3 Method

The diffusion of two immiscible electrolytes in separators was investigated with Raman spectroscopy. Out of the immiscible pairs found in literature and tested positive for their immiscibility, two were selected for the Raman measurements, DBE and [PYR14][TFSI] as well as [P_{66614}][TFSI] and [Emim][TFSI]. Since [Emim][TFSI] does not wet Celgard it was decided that a setup with two glass fibres and a second setup with one glass fibre and one Celgard would be tested. For DBE and [PYR14][TFSI],

one setup with two glass fibre separators and a second with two Celgard separators were measured. A specific *in situ* Raman cell, meant for measurements on cells while cycling was repurposed and used with only separators. The separators were filled up with the different electrolytes and measured under various conditions, such as after pressured was applied and after some resting time. The following sections detail the method and practicals of the experiment, such as preparation of the samples and settings of the Raman spectrometer.

3.3.1 Preparation of the electrolytes and separators

The electrolytes were prepared in the same way as they would be for cycling purposes and all handling of the salt and solvents took place in an argon-filled glovebox until the sealed cell was taken out for measurements. Therefore, both solvents and salts were dried to remove moisture that could hinder the performance of the cell. LiTFSI was chosen as the lithium salt, partly due to it being well documented in literature in relation to the chosen solvents, but also due to the usage of $[TFSI]^-$ as an anion in the ILs. The salt was dried in a Büchi oven under vacuum and at 120°C, for 24 hours. Likewise, the solvents were dried in a Büchi oven but at slightly varying temperatures. [PYR14][TFSI] (From Solvionic), DBE (Sigma-Aldrich) and [Emim][TFSI] (Solvionic) were all dried at 100°C for 24 hours. $[P_{66614}]$[TFSI] (Sigma-Aldrich), had a documented flash point of 52°C and was dried at 50°C for 24 hours. It is however unclear whether such a low temperature as 50°C managed to evaporate any moisture as the boiling temperature of water is slightly below 100°C. Finally, the electrolytes were mixed to a concentration of 1 M LiTFSI and stirred on a magnetic stirrer overnight. All solvents except for $[P_{66614}]$[TFSI]completely solved their salt. In $[P_{66614}]$[TFSI], small crystals could still be seen even after additional stirring under heat for a number of hours. The Celgard was of model 2400, with a thickness of 25 μm and 40% porosities. The glass fibre (Hartman GF/C) had a thickness of 260 μm and pore size of 1.2 μm. They were cut into 10 mm rounds to fit the metal piston.

3.3.2 *In situ* Raman cell

Performing Raman measurements on the materials of a cell during cycling, *in situ*, makes it possible to study the evolution of the electrode materials during intercalation and deintercalation. For instance, the insertion of lithium in graphite causes the distance between the graphene sheets to increase. This expansion and subsequent change in bond strength between the sheets can be seen as a shift of the peaks in the Raman spectrum. To gain access to the graphite surface, *in situ* Raman cells such as the one in Fig. 3.4 have been developed.

The cell stack is built in a cylindrical compartment with a metal piston at the bottom and a transparent glass pane at the top and is sealed by screwing a metal top to the rest of the cell. Contrary to regular coin cells, where the copper current collector is attached to the graphite, the *in situ* cell utilises a copper mesh between the top glass window and the graphite, ensuring good connectivity to the external circuit but still allowing the laser through the holes of the mesh. The cell has three

pins that can be screwed into the stack, connecting the electrodes to the external circuit. For the diffusion measurements the electrodes were removed as well as the copper mesh and an additional separator was added.

A spring can be added to the bottom of the cell and screwed in to push the cell stack platform against the glass. This could be done without exposing the cell to the environment as the piston had an internal packing sealing the cell. To prevent leakage, vacuum grease was applied to both the O-ring by the glass and the packing of the piston. The diameter of the piston holding the stack is 10 mm, and the separators were cut to match. Approximately 15 μl of electrolyte was added to wet the Celgard while 20 μl was added to the glass fibre. The first separator was placed in the cell dry and then wetted, while the second separator was wetted before being added on top.

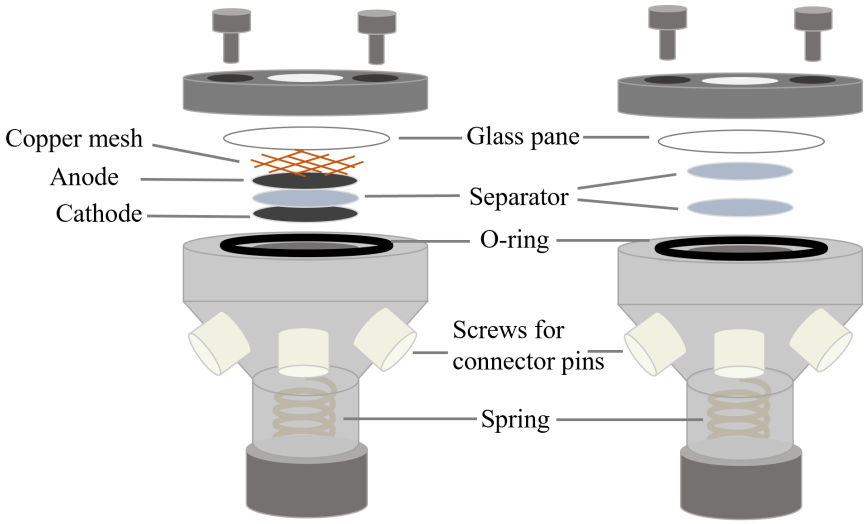

Figure 3.4: Left: Raman *in situ* cell used for cycling measurements. Right: The setup for the Raman diffusion measurements of this work.

To properly evaluate the diffusion, individual spectra of the electrolytes was taken to be used for comparison. The same cell was used for these measurements to have the same environment and parameters. Without the spring inserted in the cell, the piston could be pulled down creating a cylindrical well to hold the liquids. To prevent spillage and use less electrolyte a Teflon spacer with a small hole was added on top of the piston, creating an even smaller well to hold the electrolyte.

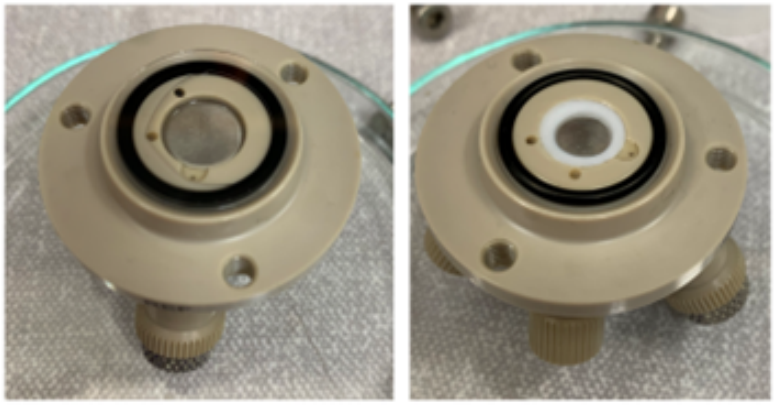

Figure 3.5: Setup for measuring the Raman spectrum of the individual electrolytes. The white Teflon spacer holds the liquid and prevents spillage.

3.3.3 Instrumental setup, calibration and focusing

A LabRAM HR Evolution Confocal Raman Microscope from Horiba was used, with a HeNe laser of wavelength 633 nm (red HeNe) from REO. During the first trial measurements a blue laser of wavelength 488 nm from Coherent was used to investigate if the fluorescence from the sample was less. Although the fluorescence was reduced slightly, the signal was weaker due the less energetic photons, making it necessary to take longer measurements which, compared to the red laser, was noisier. Furthermore, two diffraction gratings of 300 lines/mm and 1800 lines/mm were tested, before choosing the 300 grating due to faster measurements, and relatively similar energy resolution. The size of the pinhole was set to 199 μm, while objectives with magnifications 10x (NA 0.25) and 50x (NA 0.50) were used. Before measurements the spectrometer was calibrated with a 100x objective using a silicon sample which shows a clear recognisable peak at 520 cm^{-1}. The calibration was done automatically by the LabSpec 6 software used with the LabRAM.

The cell was placed in plastic holder on a movable platform below the objective and the laser beam was focused on the surface of the separators by moving the platform and cell along the three axes. A camera behind the objective fed image to the LabSpec 6 and making it possible to see where the focus of the laser was. Given the transparent nature of the Celgard it was possible to focus both on the top surface of the Celgard and then adjust the focus further down. Images from the spectrometer camera can be seen in Fig. 3.6. The texture of the Celgard was finer with smaller fibres while the glass fibre had a shinier surface with larger fibres. The wet glass fibre was however not transparent enough to find a focus further down. In the case of two stacked, wetted, Celgards the metal surface of the Raman cell could be seen through the separators. Before pressing the stack of Celgard, both surfaces could be distinguished and focused on. When pressed, they stuck together and to the bottom of the glass pane, making focusing harder. As a solution, the focus was placed just below the bottom of the glass which had a distinct structure making it easy to locate. The measurements were taken with the doors of the spectrometer closed.

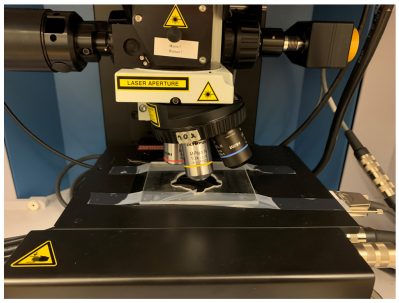

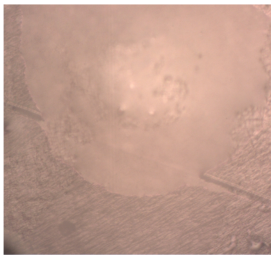

Focus on Celgard

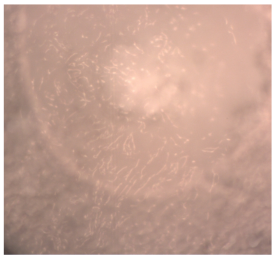

Focus on glass fibre

Figure 3.6: The measurement platform with a plastic holder for the cell. Camera images from the spectrometer of Celgard on glass fibre, both separators wetted.

3.4 Results

Four setups were measured, a glass fibre/glass fibre and Celgard/Celgard stack for DBE and [PYR14][TFSI], and a glass fibre/glass fibre and Celgard/glass fibre stack for $[P_{66614}]$[TFSI] and [Emim][TFSI]. All spectra were processed before being plotted. A background function was fitted individually to each spectrum and the intensity of the peaks scaled the same for easy comparison, while small lateral shifts were added to distinguish between spectra more easily. The relative intensity of the peaks is dependent on the concentration as well as the scattering properties of the molecules [66].

LiTFSI was present in all electrolytes although sometimes emitted in the captions or legends due to lack of space. Moreover, areas of interest in the spectra are the locations of peaks that only appear for one of the electrolytes as that will make it possible to differentiate between the molecules present. Some peaks the electrolytes will share due to it being a bond shared by molecules in the solvents, such as methyl ($-CH_3$), or the functional groups of the LiTFSI. Therefore, the plotted graphs are split into smaller ranges, excluding areas where no peaks are visible, or where the peaks are located at the same shift.

3.4.1 Baseline fit

Due to fluorescence and the inelastic scattering being a relatively weak signal, there is often a significant baseline in Raman spectra. However, since this background is added to the signals from the Raman scattering, it does not hide the peaks but only adds to them. Therefore, it is relatively simple to remove the background and make the peaks more visible. In this work a 4th degree Huber function was fitted to the background using the MATLAB function `backcor.m` [71]. The chosen function gave the closest fit when compared to other functions and degrees. A baseline fit of a measurement of 1 M LiTFSI in $[P_{66614}]$[TFSI] can be seen in Fig. 3.7

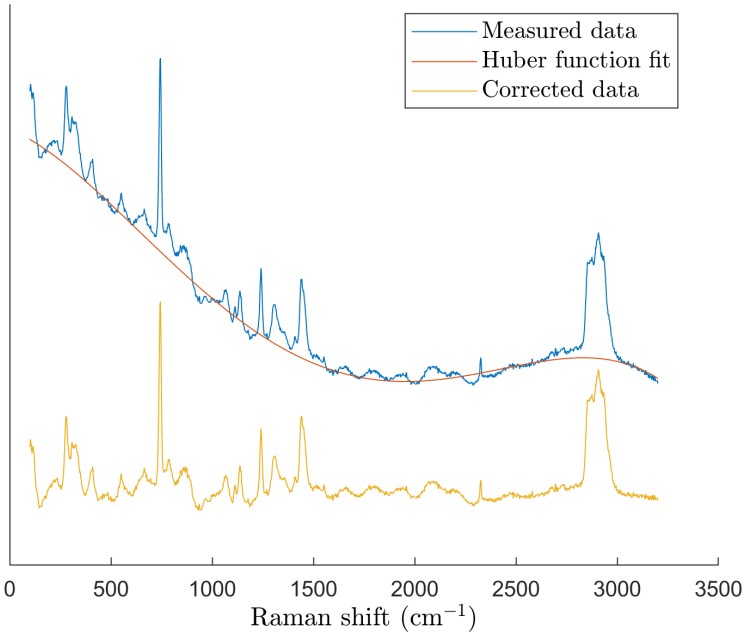

Figure 3.7: Correction of the measured Raman spectra of 1 M LiTFSI in $[P_{66614}][TFSI]$ by fitting a 4th degree Huber function to the background.

3.4.2 [Emim][TFSI] and $[P_{66614}][TFSI]$

The individual electrolytes were measured with the 50x objective as it was easier to focus on the bulk liquids. It proved difficult however to find and focus on the surfaces of the separators, leading to the 10x objective being used for all surface measurements. The spectra of measurements made of the glass fibre stack can be seen in Fig. 3.8. Measurements of an unwetted glass fibre was also taken but practically no peaks were visible, hence it is not included. Given that [Emim][TFSI] has a higher density, it was applied to the bottom glass fibre. Without pressing, the measured spectrum looks practically identical to $[P_{66614}][TFSI]$, indicating no immediate diffusion of [Emim][TFSI] to the top. Likewise, after inserting the spring and focusing on the glass fibre surface pressed against the glass pane, no traces of [Emim][TFSI] could be detected.

The cell was thereafter left for 24 hours before repeating the last measurement. At 600 cm^{-1} and 1025 cm^{-1} there might be some small traces of [Emim][TFSI] peaks, although not clear enough to be certain it is peaks forming. When the separators were soaked the high viscosity electrolytes took a long time to reach the edges of the glass fibre. During assembly it was suspected that the $[P_{66614}][TFSI]$, did not entirely reach the edges of the separator before it was placed on top of the [Emim][TFSI]. In consideration of this, a final measurement of the edge of the separator was done. Contrary to the other measurements, here the presence of [Emim][TFSI] is obvious as well as the presence of $[P_{66614}][TFSI]$. Based on the improper wetting during the assembly, the most probable cause would be the diffusion of lower viscosity [Emim][TFSI] up into the empty pores at the edge.

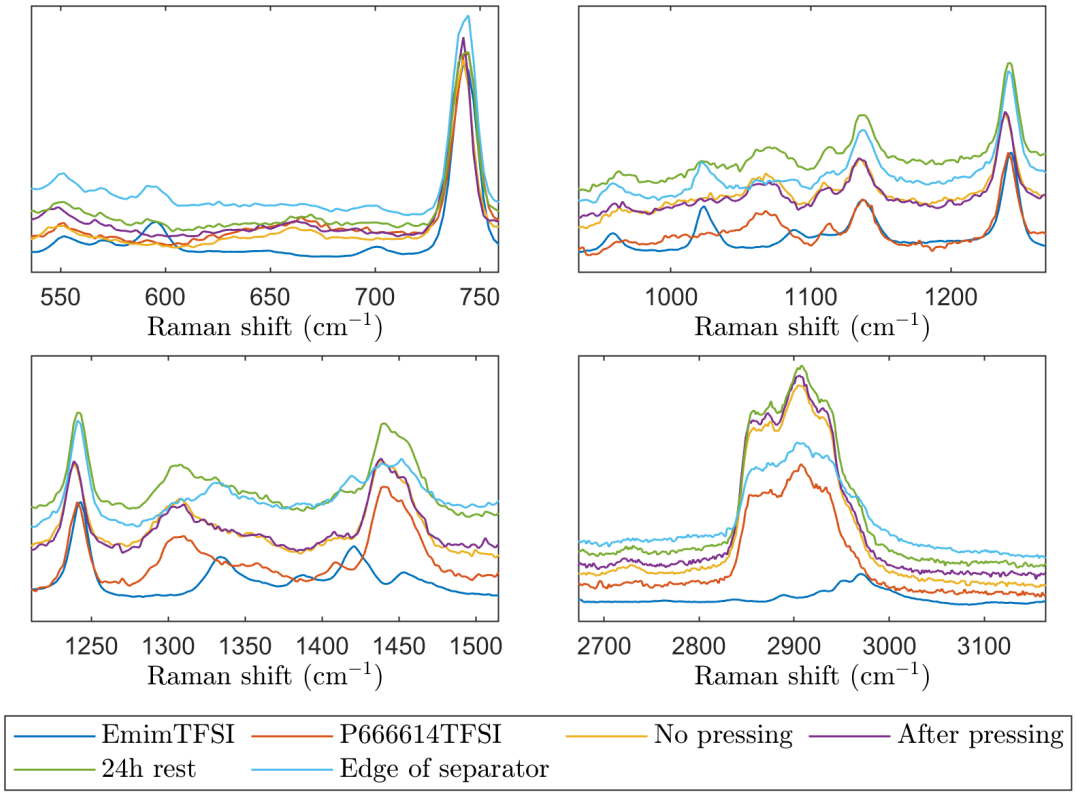

Figure 3.8: Raman spectra of a 1 M LiTFSI in $[P_{66614}][TFSI]$-soaked glass fibre separator in contact with a 1 M LiTFSI in [Emim][TFSI]-soaked glass fibre separator, with the former being on top.

As for the previous separator setup, the 10x objective was used to measure the $[P_{66614}][TFSI]$-soaked Celgard against the [Emim][TFSI] glass fibre separators (Fig. 3.9). Contrary to glass fibre, Celgard has a distinct Raman spectrum with few peaks coinciding with [Emim][TFSI] or $[P_{66614}][TFSI]$. At 740 cm^{-1} and 1250 cm^{-1} two clear peaks are visible, belonging to LiTFSI. Given that [Emim][TFSI] cannot wet the Celgard on its own, the diffusion into the top separator is presumed unlikely. Since the Celgard became close to transparent when wetted, focus was placed on both the Celgard and glass fibre surface. However, these two measurements, taken before pressing the separator have an almost identical appearance. Furthermore, the peaks both coincide with the peaks for Celgard and [Emim][TFSI], but not $[P_{66614}][TFSI]$, which is unexpected. The occurrence of [Emim][TFSI] in both these measurements strongly suggests that the depth resolution in wetted Celgard is wider than the thickness of the separator.

The measurement after pressing only brought the stack closer, resulting in this spectrum being identical to the two measurements of the unpressed stack. The hypothesis that it is the transparency of the Celgard which is responsible for the visibility of [Emim][TFSI] and not diffusion, is seemingly confirmed by the measured spectrum of the Celgard separator on its own. After opening the cell under a fume hood, carefully removing the bottom glass fiber and placing the Celgard back in the cell without the spring, a final measurement was made. Evaporation of the electrolyte was not deemed an issue simply due to the low vapour pressure of ILs,

meaning the probability of molecules escaping the liquid is very small. This spectrum showed almost exclusively Celgard peaks while there were no traces of [Emim][TFSI] since the 600 cm^{-1} and 1425 cm^{-1} peaks disappeared after the removal of the glass fibre. Instead, some additional peaks appeared, for instance at 1440 cm-1 and 1300 cm-1 that does not seem to belong to Celgard but [P_{66614}][TFSI]. However, the origin of peak at 1160 cm^{-1}, is still unclear. Possibly, the metal piston visible through the electrolyte could be the cause.

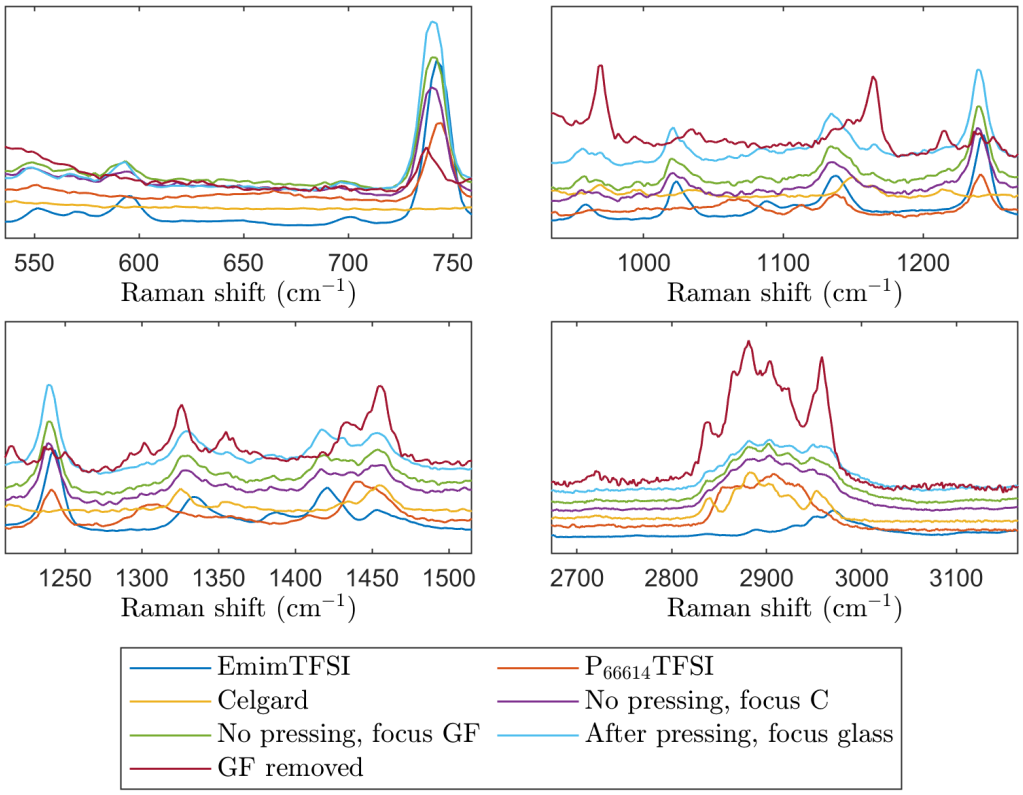

Figure 3.9: Raman spectra of a 1 M in LiTFSI in [P_{66614}][TFSI]-soaked Celgard separator in contact with a 1 M LiTFSI in [Emim][TFSI]-soaked glass fibre separator, with the former being on top.

3.4.3 [PYR14][TFSI] and DBE

Analogous to the first electrolyte pairs, the Raman cell was assembled by first wetting a glass fibre placed on the metal piston with [PYR14][TFSI]. Thereafter another glass fibre was entirely wetted with DBE before being placed on top of the first. As for the other pair, all surface measurements were made with the 10x objective and the electrolytes alone with the 50x. In comparison with the ILs however, the spectra for DBE as well as the spectra containing it, appeared noisier. Without pressing, the measured spectra seem to only contain DBE. The [PYR14][TFSI] peak at 900 cm^{-1} is missing while the DBE peaks at 850 cm^{-1}, 1300 cm^{-1} and 2900 cm^{-1} are clearly visible. However, after pressing the separators these three peaks immediately disappear and the broad peak at 2900 cm^{-1} starts to look like the ones for [PYR14][TFSI]. The measuring time after pressing was only 10 minutes so the diffusion happened

relatively fast.

After letting the cell rest for 24 hours, the final spectrum only showed very small indications of DBE at 470 cm^{-1}. At this stage the top of the DBE-soaked glass fibre looked dry. The volatility and fast evaporation of DBE seems to be a problem and the reason for the diffusion of [PYR14][TFSI] into the top electrode, in the same way [Emim][TFSI] could diffuse and the dry edges of the separator. A drawback of the Raman cell is the large open space under the glass plane. Immediately after assembly and when looking at bottom of the glass through the spectroscopy camera, droplets of DBE could be seen that had evaporated from the separator. Even though the evaporation of DBE may be an issue in a normal cell as well, probably not to the extent of the Raman cell, making these measurements unreliable. It cannot be determined if the diffusion of [PYR14][TFSI] was due to the mixing of the electrolytes and subsequent drying of DBE, leaving the PYR14][TFSI] in the separator, or if evaporation of DBE took place before the diffusion. However, given what was observed for [Emim][TFSI], the latter seem more plausible.

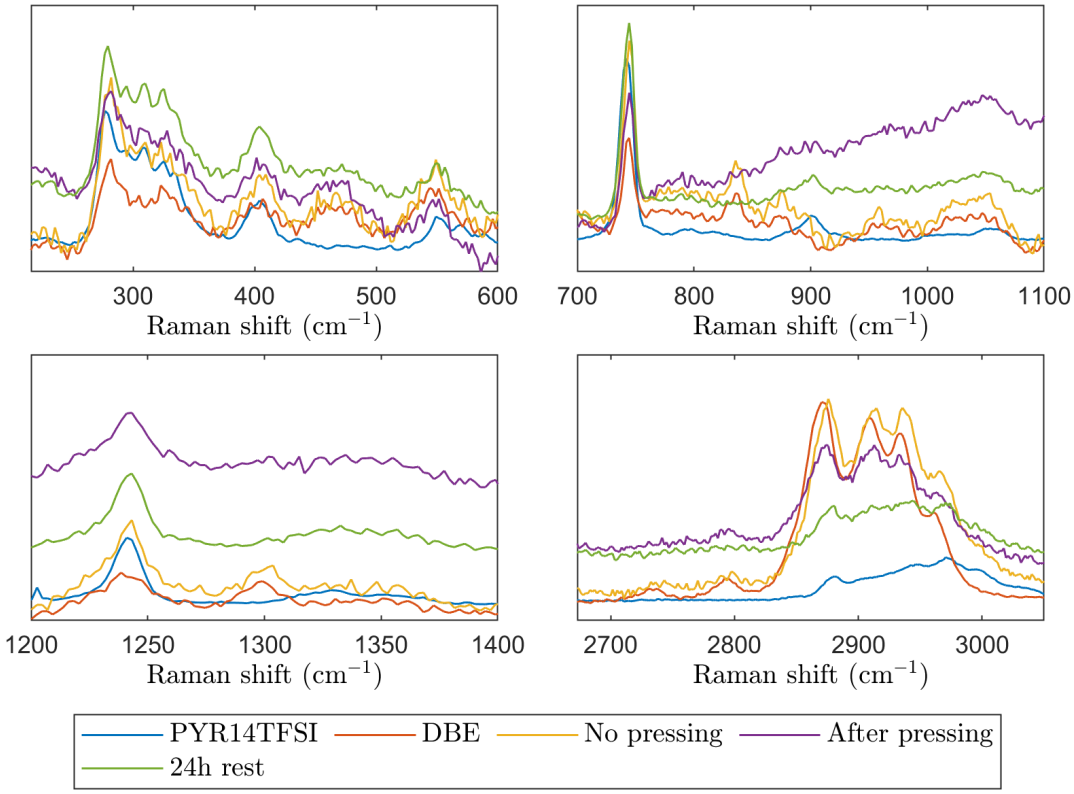

Figure 3.10: Raman spectra of a 1 M LiTFSI in DBE-soaked glass fibre separator in contact with a 1 M LiTFSI in [PYR14][TFSI]-soaked glass fibre separator, with the former being on top.

The final measurement setup was of two Celgard separators and as for the IL pair, the top Celgard was transparent enough to allow for focusing on the surface or the bottom Celgard. However, like the IL pair the transparency of the separator seems to worsen the depth resolution, meaning scattered photons from the entire separator stack is included. Looking at spectrum, it is instantly noted that the

spectra all look very similar. As for the Celgard and glass fibre stack for the ILs, the ”no pressing” and ”pressing” look near identical, and the same for the 24-hour measurement. At first glance, it looks like they all include the DBE peaks. However, due to the similarities between the molecular structure of DBE and Celgard, almost all of DBE's peaks are covered by Celgard, making it hard to determine if the former is present in the separator. The peaks around 300 cm^{-1} and 750 cm^{-1} Celgard lack are instead covered by the LiTFSI. The surface of the Celgard was surprisingly enough not dry. However, since the Celgard is thinner than the glass fibre, it is more likely that [PYR14][TFSI] had permeated the Celgard than DBE not having evaporated.

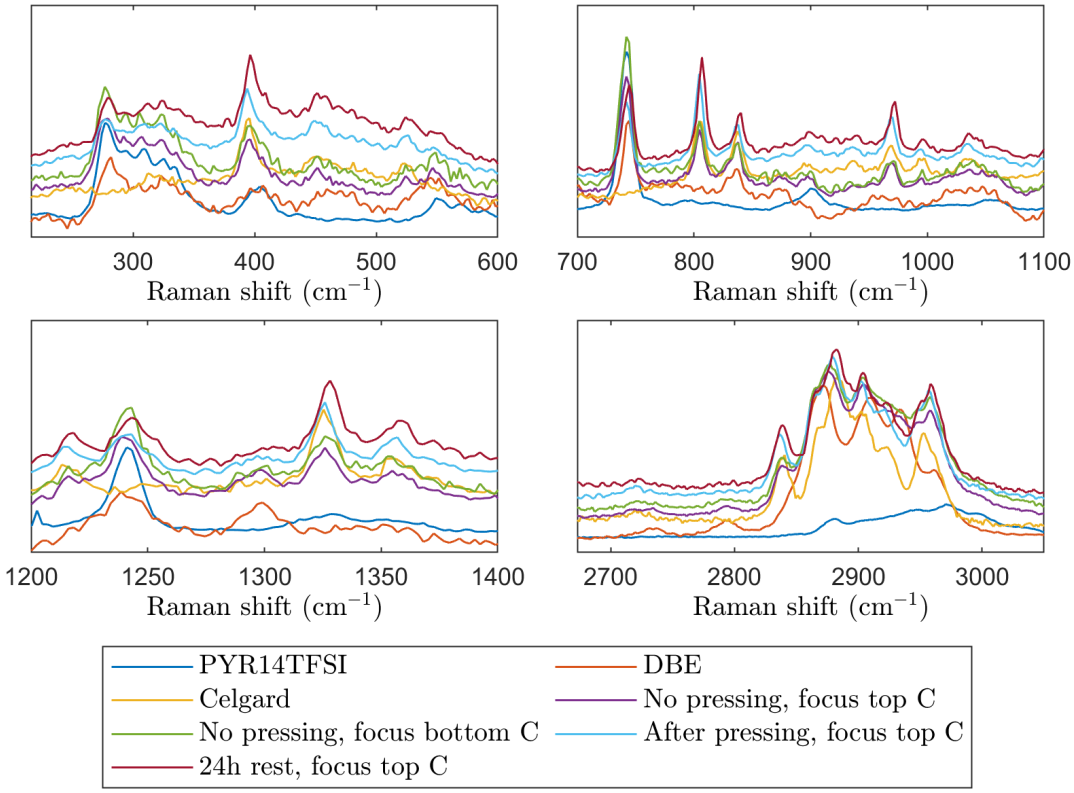

Figure 3.11: Raman spectra of a 1 M LiTFSI in DBE-soaked Celgard separator in contact with a 1 M LiTFSI in [PYR14][TFSI]-soaked Celgard separator, with the former being on top.

3.4.4 Discussion

As was expected beforehand, the depth resolution of the transparent wetted Celgards was an issue, with the scattered signal coming from points all throughout the sample. Unfortunately, performing measurements with the 100x or 50x objectives were difficult due to the lack of easily recognisable structures to focus on when the separators were wet. Less light is let through these objectives also making it hard to find focus. It would have been interesting to determine the depth resolution of the 10x objective by adding a recognisable background to the sample, like silicon or another denser polymer as was done in the Tabaksblat article [69] to see at which

depth the background could be detected. The LabSpec 6 software has a mapping function for confocal Raman measurements, taking measurements at points while automatically moving the platform to form a three dimensional scanning of the sample. However, due to time constraints, this function was not utilised in this work. Celgard separators could be stacked to form a larger sample.

However, the mapping would take longer which is a problem when measuring the more volatile solvents such as DBE. Alternative cell setups should be investigated where there is less open space for the solvent to evaporate. Perhaps some type of electrode-like material with a small hole for the laser beam, to further emulate a real coin cell, would be suitable. The contact with the electrode would decrease the area of evaporation and give a more even pressure to the stack. The longer measuring times would also mean a risk of diffusion happening faster than the measurement. Typically, the spectra was taken with an acquisition time of 60 s and an accumulation of 5, resulting in a total measuring time of just over 10 minutes since the grating demanded the spectrum to be divided into two parts. This is a short time scale in comparison to the mapping where a measurement like this needs to be taken for each point of interest.

Moving on, there are several measurements that would have been interesting to perform if given more time, for example the inverted electrolyte configuration. Perhaps gravity would eventually switch the electrolytes back, or maybe the capillary forces would contain the liquids within the separators. A cell where the pressure could be controlled more easily would also be desirable. The Raman cell offered only two, without spring (no pressure) or with. Furthermore, it is unclear how similar the pressure of the Raman cell is to a coin cell since the electrodes have been removed.

Finally, a note should be added about the oscillating patterns visible in many of the acquired spectra, for example in the baseline example (Fig. 3.7). The waves were most visible in the 1500-2250 cm^{-1} region as few peaks were situated there. It is possible that they were hidden in the background at other wavelengths too. The waves appeared for some of the measurements, regardless of if they were in liquid, solid or semi-liquid form as for the wetted sepators. Initial theories were that they were from the metal background, however steel does not produce these peaks. Moreover, the waves were more visible when the overall signal was weak and noisy. Due to its oscillating nature, it would be reasonable to think that it is some kind of interference between reflective surfaces in the cell, perhaps between the liquid, glass pane or metal piston. The period of the peaks were approximately 140 $^{-1}$ and was the same for all measurements with the 633 nm laser. They were not visible for some measurements of Celgard made with the 488 nm laser, however they were not visible for the 633 nm measurements of Celgard either. Using Bragg's equation an approximate length scale could be estimated:

$$d = \frac{n\lambda}{2\sin\theta} \approx \frac{1}{2 \cdot 140 \cdot 1}\mathrm{cm} = 35\,\mu\mathrm{m} \tag{3.3}$$

where the incidental angle θ of the laser is taken to be $\pi/2$. This distance could be the thickness of a separator or perhaps the glass that the laser light bounces off.

4

Dual electrolyte cell characterisation

The aim of all battery research is to produce cells and batteries that can cycle reliably, with high capacity retention and stable voltage output. Many parameters, both internal, such as choice of materials, and external, such as temperature and pressure, will affect these properties. The commercialisation process of a battery is detailed and the cell is tested in many settings and configurations to find the optimal performance. After finding promising materials showing desirable properties, the first step is to test them in a battery under simple conditions and on a small scale, such as in a coin cell or in the lithium half-cell configuration presented in Section 2.4.3.

This chapter investigates the electrochemical properties of the electrolytes found in the immiscibility study. It begins by explaining the basics of cell cycling and the relevant properties of a battery cell, as well as desirable behaviour. Thereafter, electrochemical techniques such as linear sweep voltammetry (LSV) and galvanostatic cycling (GC) is presented and connected to the reactions inside the cell. Finally, the preparation of cell materials for cycling and the equipment used is detailed before the results of the cycling of LNMO/graphite cells with the selected electrolytes are presented.

4.1 Theory

The basics of the electrochemical reactions taking place inside a cell and the kinetics of the charged particles have been presented in Chapter 2. Here, the cell will be treated in its entirety with the focus being on the overall performance and parameters of the cell. An ideal battery will supply a constant and even potential to an attached load until it is fully discharged. First, this section will take a look at the different definitions of voltages that exist in the battery realm. Thereafter, the most common variables and terms used to characterise the cycling performance will be presented. These values can be gathered with different cycling methods, which often includes varying the voltage of the cell and measuring the induced current, or vice versa.

4.1.1 Voltage response

The theoretical voltage output of a cell will be given by the properties of the electrodes. It can be approximated by taking the difference in redox potential of the

cathode and anode active materials relative to some standard reference electrode, which in the case of LIBs often is taken to be lithium metal. For example, (Table 2.1) 4.7 V for LNMO and 0.1 V for graphite, giving a theoretical cell voltage of 4.6 V. The theoretical voltage is usually close to the experimental *open cell voltage*, that can be measured between the anode and cathode just after assembly [5]. However during cycling the voltage output, also known as the *operating voltage* is usually lower. This is partly due to Ohmic losses in the battery, simply calculated by $V = R \cdot i$ and subtracted from the voltage. Furthermore, the polarisation discussed in Section 2.2 will also lead to a loss of voltage as the accumulation of charged particles at the interface will create an opposing potential [72]. The difference between an ideal battery and a practical, but still optimistic, one, is demonstrated in Fig. 4.1. The stable voltage in the nominal region is naturally called the *nominal voltage*, and is the value most often given for commercial batteries.

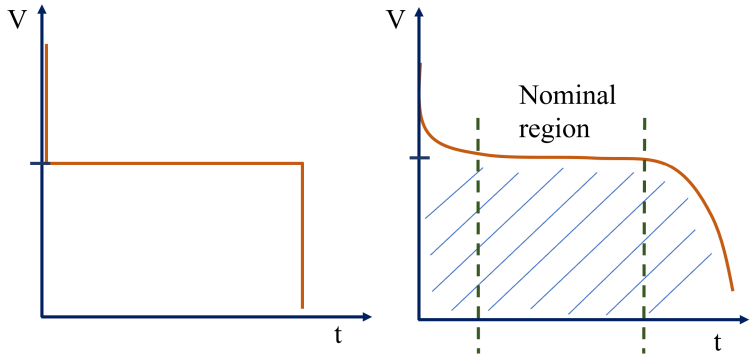

Figure 4.1: Differences between an ideal voltage response and a more realistic discharge curve.

4.1.2 Characterisation of cells

The arguably most important parameter of a battery is its Faradaic capacity, given by

$$C = \int i \mathrm{d}t \tag{4.1}$$

where i is the current measured at the electrode. It is measured in Ampere hours (Ah) and will give the amount of charge stored in the anode and cathode during cell operation.

Another important parameter when cycling is the *C-rate* or charge/discharge rate. As every electrode will be different in terms of mass, theoretical capacity and surface area, it is common to specify the rate of charge in terms of a electrode dependent variable C instead of a specific current. The C value of an electrode is given by the maximum capacity either calculated from the specific capacity or the area capacity. For instance, given a 10 mm diameter LFP electrode of area capacity 2.0 mAh/cm^2, the 1C rate is simply

$$C = 2.0 \cdot 0.5^2 \cdot \pi = 1.57\,\mathrm{mA} \tag{4.2}$$

Applying the current $1\,C$ it would mean that the cell would be fully charged in one hour. Similarly, with a rate of $C/10 = 0.157$ mA it would instead take 10 hours for

the cell to be fully charged. To ensure the formation of a good SEI, it is common for commercial electrodes to come with a recommended cycling protocol. An example is the LFP from Customcells ([8]),

1. 2 cycles (charge and discharge) with $C/10$
2. 2 cycles with $C/5$
3. cycling with 1C

where each charging entails first applying the constant current as specified by the steps and then a subsequent constant voltage hold until the current across the battery reaches the current of $C/10$.

The storing capabilities of the electrodes and the capacity will gradually reduce as the cell is cycled. A few common reasons are a loss of active material due to the formation of the SEI, decomposition of the electrolyte and structural changes to the electrode causing it to lose storing capability. The *capacity retention* is the ability of the cell to maintain the capacity over cycles. Another measure is the *Coulombic efficiency* of a charge/discharge cycle. It is the ratio of charge supplied to the cell during charging and the charge that can be taken out during discharge. A loss of charge, leading to a efficiency less than 1, would indicate the loss of charged particles to parasitic reactions within the cell such as the SEI, decomposition and gas formation [17].

4.2 Cycling of cells

There are multiple techniques and methods to evaluate the performance of cells. The most common include sweeping the voltage over a range while measuring the current at the cathode (voltammetry) or applying a constant current while measuring the voltage at the electrode (galvanostatic cycling). In this section the chemical reactions inside the battery is connected to the current and voltage outputs of the cell during cycling in order to better understand the characteristics of the graphs and to be able to draw conclusions about the internal chemical reactions.

4.2.1 Linear sweep voltammetry

The linear sweep voltammetry consist of a single sweep of voltage across the cell from one value to another, either from high to low or low to high by using a potentiostat. With a changing voltage, redox reactions will take place in the cell, resulting in spikes of current at particular voltages. Theses spikes are interesting to study to see at which voltage the materials of the cell will interact. The LSV is particularly useful in studying the decomposition of the electrolyte, as the decomposition reaction will add to the normal current from the electrode/electrolyte redox reactions and be visible in the I/V diagram. To study this the cell is normally swept from low potential at the cathode to high, to see at which voltage the decomposition starts.

As mentioned in Section 2.1, a current will begin to flow between the electrodes as an overvoltage is applied on the cell. The initial current will exhibit linear Ohmic behaviour, but eventually there will be an accumulation of charged particles at the anode interface due to the increasing voltage, resulting in an opposite potential. The current will therefore reach a equilibrium plateau, and be stable. Finally, there

will be no more lithium ions to transport across the electrolyte. However, a current will still run between the electrodes due to Ohms law, and the resistance across the battery. This can be seen as sharp increase of the current at the end of the voltage range.

Additionally, although not used in this work, except for in the recommended cycling protocol of LFP, cyclic voltammetry (CV) should be mentioned briefly. LSV constitutes the first half of CV, which is a cyclic sweep from one voltage to another and back again. The CV gives information about the reversibility of the cell and can also give details on the nature of the bonds and charge transfer between the molecules in the battery, by studying how the peaks in current vary between sweeps [73].

4.2.2 Galvanostatic cycling

In galvanostatic cycling (GC) (or chronopotentiometry) the current is kept constant and the induced voltage is measured at the cathode. A positive current is applied to the cell, triggering an oxidation of lithium at the cathode and a reduction at the anode. This will gradually increase the voltage across the cell as lithium is intercalated into graphite, or plated onto lithium. The consumption of lithium at the anode will create a concentration gradient inducing an opposing potential as for the case of LSV. Therefore a nominal stable voltage across the cell is reached. Eventually there will be no more available lithium for reduction at the anode. Once again the behaviour will turn linear and Ohmic [17].

When establishing a GC cycling protocol a constant current is decided based on the C-rate, or example $C/10$. The current will be applied to the cell and the voltage recorded. A cut-off voltage is defined which after being reached, prompts the inverting of the current, now flowing to the cathode. The cut-off voltage is usually defined by the electrode manufacturers and given on the data sheet. After the current has been inverted the opposite procedure takes place with a voltage plateau being reached before the current spike in the Ohmic region. A lower cut-off voltage is also defined and upon being reached the direction of the current once again switch. Normally the charge rate and discharge rate is the same, while the rate between cycles may vary. As for the LFP protocol, it is normal for the first cycles to be cycled slower in order for a proper SEI to form.

During the cycling the voltage is measured as a function of time and voltage. Although in some cases it might be interesting to study the voltage as a function of time, GC measurements are often presented with charge/discharge curves as a function of capacity. The capacity cannot be measured directly but is instead calculated cumulatively with Eq. 4.1, the time integral over the current. Since the current is constant this is rather easy, and the capacity will directly proportional to the time, but the cycling softwares usually do this directly. It is also common to have the capacity axis be in units of specific capacity (mAh/g) as comparisons between electrodes with different area and amount of active material will be easier. Normally the weight of the active material can be added straight into the cycling software. The weight is calculated by weighing the electrode, removing the weight of the current collector foil and multiplying it with the percentage of active material

in the coating, subtracting the weight of the binder.

The charge and discharge curves are split into two as can be seen in later sections. This way of presenting data is very common and give a lot of information. For example, the coulombic efficiency can be seen as the difference in capacity in between where the charge curve ends and the discharge curve begin. Furhermore, the capacity retention can also easily be spotted as the cell cycled by observing where the capacity curve begin.

4.3 Method

Coin cells were assembled and cycled at the Material Physics laboratory at Chalmers. The preparations included the drying of all the cell materials to remove moisture that could potentially hinder the performance of the cell. The data, dimensions and manufacturers of the materials are given in the beginning of this section followed by a description of the cycling protocol used for the various cells. Lastly the cycling equipment used is briefly presented.

4.3.1 Preparation of materials and cells

The electrolytes had already been dried and prepared for the immiscibility study and were used as they were. The commercial electrolyte EC:DMC (50:50) 1 M $LiPF_6$ was from Sigma Aldrich and was used as is was. The second addition was the fluorinated ethylene carbonate (FEC) (Sigma Aldrich) that was dried at 120° C for 24 hours before mixed with LiTFSI at a concentration of 1 M. It was thereafter added to DBE and [Emim][TSFI] at a 2% wt (weight percent). Furthermore, the DBE/FEC and [Emim][TSFI]/FEC mixtures was mixed with [PYR14][TFSI] and $[P_{66614}]$[TFSI] respectively to ensure they were still immiscible, which was confirmed. The electrodes used; LFP (Customcells), graphite (Customcells), and LNMO (Morrow Batteries) were all cut into 10 mm rounds dried at 110°C, in a Büchi-oven overnight. As the electrodes have a tendency to curl when dried, they where placed between glass panels and clamped while in the oven. The same separators as for the diffusion measurements were used, but only glass fibre was ended up being used due to it being easier to soak. They where cut slightly bigger at 14 mm to avoid short circuiting the cell if the electrodes were placed off-centre. They were thereafter dried in a vacuum oven at 90°C as recommended by the data sheets. Approximately 60 μl electrolyte was added to each 14 mm glass fibre separator.

Some data for the electrodes are given in Table 4.1. For the LSV, a graphitic carbon was used as anode opposed to platina, which is commonly used for other cathodes, due to the reported poor correspondence with the actual oxidation potential [74]. Since no intercalation would take place at the anode, the only important property of the graphitic carbon was its electrochemical stability. The coin cells were assembled and sealed inside an argon-filled glovebox as showed earlier in Fig. 2.5. For the cells with lithium metal as anode, the soft metal was stamped into 14 mm rounds and brushed on both sides with a plastic brush to remove any potential oxidation on the surface. It was thereafter stuck to the coin cell ring and assembled with the rest of the cell.

An alternative setup without separators were introduced at a later stage in the cycling experiments, to see if mixing and contact of electrolytes were an issue of the separators and not of the immiscibility. Swagelok cells were used together with a Teflon ring of the same type as the one used in the Raman cell (Fig. 3.5). The electrodes were placed in contact with the metal pistons as normal but instead of a separator, the Teflon ring was placed directly onto the bottom cathode. The hole was filled up halfway of the denser electrolyte before filling up the rest with the second electrolyte. The cell was allowed some time for the bottom electrolyte to seep underneath the ring and wet the cathode before more of the second electrolyte was used to fill up the Teflon hole to the brim with surface tension. The anode was then placed on top the ring, ensuring that contact was made with the electrolyte. The other pistons was thereafter added an the cell compressed until it was stopped by the width of the ring. In this cell, only the electrolyte separated the electrodes but the ring made short circuiting impossible. Furthermore, it was kept upright during transfer out of the glovebox as well as during cycling as not to disturb the electrolytes.

Table 4.1: Data for the commercial electrodes used for cycling.

Type	**Spec. capacity (mAh/g)**	**Area capacity (mAh/cm^2)**	**Nominal voltage (V)**	**Manufacturer**
Graphite	355	2.4	0.10	Customcells [37]
LFP	150	2.0	3.4	Customcells [8]
LNMO	- (93.5 wt% active material)	1.982	-	Morrow Batteries

4.3.2 Cycling protocol

The benchmark LFP/G was cycled in accordance with the protocol in Section 4.1.2. Inspiration for the cycling protocol of the LNMO cells were taken from the one from LFP as well as literature recommendations for the cut-off voltages, as no recommended protocol was given for the LNMO. However, since many of the electrolytes were of high viscosity it was decided that the cycling rate would be $C/10$ for all cycles to decrease the risk for polarisation, if the mobility of the ions were poor. The cut-off voltages for LNMO was set to 3.5 V for discharge and 5 V for charge. For cells with graphite against lithium it was set to 0.01 V and 0.7 V, as recommended by the data sheet. Furthermore, the cells were all allowed to rest a minimum of two hours before cycling to ensure good contact between the all the components as well as letting the open circuit voltage stabilise.

4.3.3 Cycling equipment

For all measurements except the LFP/G cell, a VMP3 Multichannel Potentiostat from BioLogic was used together with the EC-lab battery cycling software. For the LFP/G cell, the Scribner 580 Battery Test System was used with the Bcycle software. Some cells were cycled in a temperature controlled chamber from Vötsch

of model VT 4011, when a cycling temperature different from the room temperature was desired. The coin cell was placed in a holder with two pins for either side of the cell, with the cathode attached to the positive connector, expect in the case of graphite versus lithium. The cycling protocol was entered into the respective softwares and was let to cycle, the shortest one for just a couple of minutes (failed cell) and the longest one for 21 days.

4.4 Results

The investigated electrolytes were tested both on their own, some in mixtures and some together in a dual electrolyte setup, with and without a separator. All the electrolytes were subjected to the same LSV sweep between 0-6 V with the rate 5 mV/s in order to compare their electrochemical stability. Furthermore, the electrolytes were thereafter cycled in a lithium half cell, either against graphite or LNMO, and some against both. Finally the most promising electrolytes were tested in a full cell of LNMO and graphite.

4.4.1 Example with benchmark materials

In order to compare the novel electrolytes with an established battery, a cell with commercial electrolytes and electrodes was assembled and cycled according to recommended cycling protocol of the LFP electrode. The voltage of the cell versus time and the voltage against the capacity of the cell are presented in Fig. 4.2 and Fig. 4.3 respectively. The different rates of the initial SEI forming cycles compared to the 1C rate used after 4 cycles, can be seen in the voltage/time plot. Moreover, the plateau at 10 h is the CV hold until a current of C/100 was reached. The voltage curves are uniform indicating stable cycling performance. To properly evaluate the cell however, it is the discharge/charge curves of Fig. 4.3 that are the most relevant. The charge curve starts from a capacity of 0 mAh/g and a voltage of 2 V and is thereafter cycled up to 4 V. During charging the capacity axis tells the charge provided to the graphite. The discharge curve starts at 4 V and 0 mAh/g moving down to the right, and now the capacity axis tells the charge returned back to the cathode. During the first charging cycle a few interesting things can be noted. Firstly, the shape of the curve is uneven and differs quite a lot from the other charging curve. Secondly, the graph goes all the way up to 160 mAh/g, a bit more than the 130 mAh/g picked out from the discharge cycle, meaning the Coulombic efficiency is less than 1. These phenomenons are both a result of the formation of the SEI layer. Lithium ions are provided to the surface of the graphite and will be consumed by the SEI forming reaction. It will therefore be ”lost” to the intercalation mechanisms in the subsequent cycles, signifying IRC. Furthermore, the decomposition reactions will induce a change in potential that will be visible in the measurements of the voltage, leading to the uneven curve.

Finally, a note of the capacity retention should be made. The maximum capacity of the cell during the first cycles is quite good, around 130 mAh/g compared to the theoretical value of 160 mAh/g. However, over the course of the cycling the curves are pushed more and more to the left loosing about 20 mAh/g after 60 cycles. This

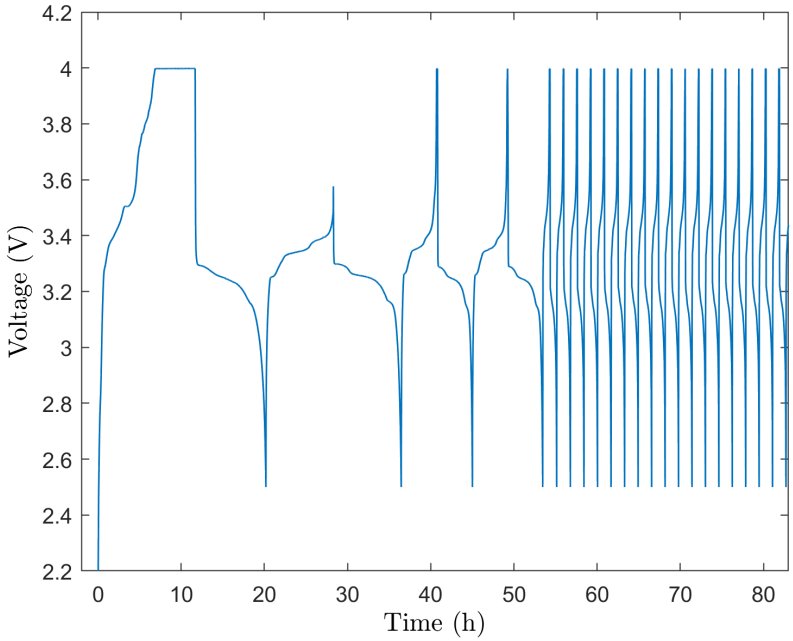

Figure 4.2: GC of an LFP/G cell with the benchmark electrolyte 1 M $LiPF_6$ in EC:DMC (1:1). The first two cycles are cycled with a current of C/10, the next two with C/5 and all subsequent cycles with 1C, in order to form a proper SEI.

parameter is very important for the performance of the cell since it determines the cycle lifespan of the cell. The possible reasons for capacity losses could for example be more decomposition of the active material of the cell, structural failure of the electrode or polarisation effects [5].

4.4.2 Single electrolyte cells

The LSV of the collection of electrolytes can be seen in Fig. 4.4. Firstly, a big decomposition peak can be seem for [Emim][TFSI] around 2.5 V meaning [Emim][TFSI] does not seem suitable against the anode and lower potentials. However, when mixed with the organic solvent FEC, which is more stable at lower voltages, this peak was compressed completely. Furthermore, [PYR14][TFSI] appeared to be the most stable at higher voltages, confirming values of 5.5 V found in the literature. When mixed with TMS the oxidation limit was slightly lowered but not significantly. The addition of FEC to DBE also seem to prevent the decomposition taking place at 3.8 V. The behaviour of $[P_{66614}][TFSI]$ was unexpected, and even after remaking the cell, the same behaviour was shown, with the current staying low even at high temperatures. Although no ESW was found for $[P_{66614}][TFSI]$ in the literature to compare it to, it was reported to be 5.81 V with another anion $[TPTP]^-$ [55]. That $[P_{66614}][TFSI]$ would be stable over 6 V therefore seems unlikely.

The Li/LNMO cells for DBE (2%wt FEC), [PYR14][TFSI]:TMS (1:1), both with 1 M LiTFSI, and the commercial electrolyte EC:DMC 1M $LiPF_6$ are presented in Fig. 4.5-4.7. Individual cells of DBE, [PYR14][TFSI], [Emim][TFSI] and $[P_{66614}][TFSI]$ with LNMO/Li were also cycled and are included in Appendix A. They will briefly be discussed here but will give way for the better performing elec-

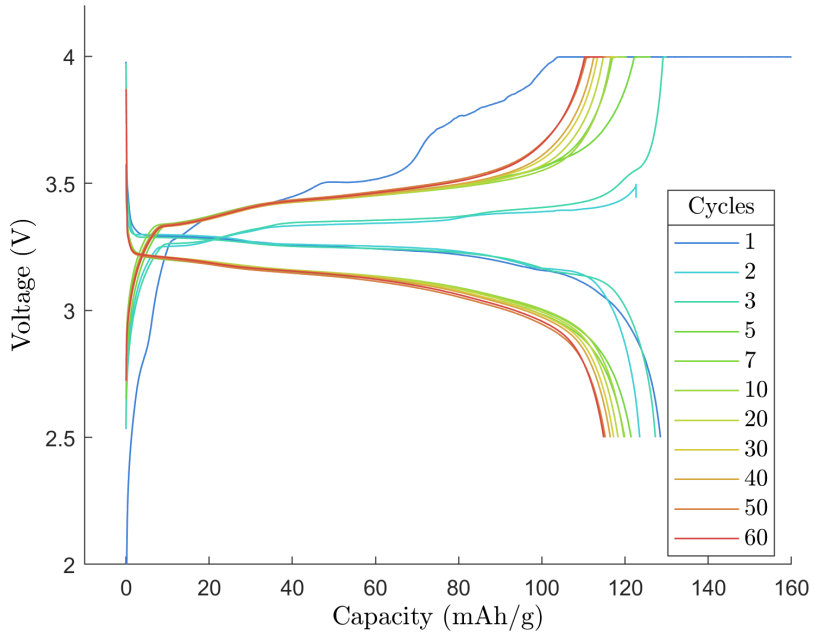

Figure 4.3: GC charge and discharge curves of a LFP/G cell with the benchmark electrolyte 1 M $LiPF_6$ in EC:DMC (1:1).

trolytes in the Results section of this work. Multiple cells with $[P_{66614}][TFSI]$ were cycled with the standard protocol, without success. Instead, the cell reached cut-off voltage immediately and quickly cycled without capacity, indicating no intercalation of lithium ions took place. The high visocity of $[P_{66614}][TFSI]$ was deemed the most probable cause, leading to severe polarisation that hindered the mobility of the ions. Furthermore, an article evaluating $[P_{66614}][TFSI]$ with 0.5 M $LiPF_6$ ([75]) came to the conclusion that the IL was incapable of forming a CEI against LNMO, although working better against LFP. Furthermore, it was stipulated that $[P_{66614}][TFSI]$ also could not form a proper SEI against graphite in a Li/G cell and that the layer was too thick and impenetrable. Likewise, the performance of [Emim][TFSI], although being able to cycle a number of cycles, the capacity retention was very poor falling from 175 mAh/g to 25 mAh/g after only three cycles. The low stability and the high viscosity [Emim][TFSI] were deemed the issue here as well. No measurements of [Emim][TFSI] together with FEC was performed as the [Emim][TFSI] fell away together with its immiscibility partner $[P_{66614}][TFSI]$.

[PYR14][TFSI] showed better cyclic stability than its fellow ILs being able to be cycled for 42 cycles at a low capacity, with the capacity actually increasing until some type of decomposition mechanism seems to have stopped the cell. Once again, the high viscosity was deemed an issue, Another [PYR14][TFSI] was cycled at 60°C to see what a decreased viscosity would mean for the performance of the cell. The results are also included in Appendix A, showing stable cycling for 6 cycles, but a quickly decreasing capacity. Instead it was the mixture with TMS (Fig. 4.5) that showed the best performance by far. The cell cycled for 6 cycles with very little loss of capacity compared to the other [PYR14][TFSI] and ILs. The capacity was 135 mAh/g which is not far from the theoretical capacity of 147 mAh/g.

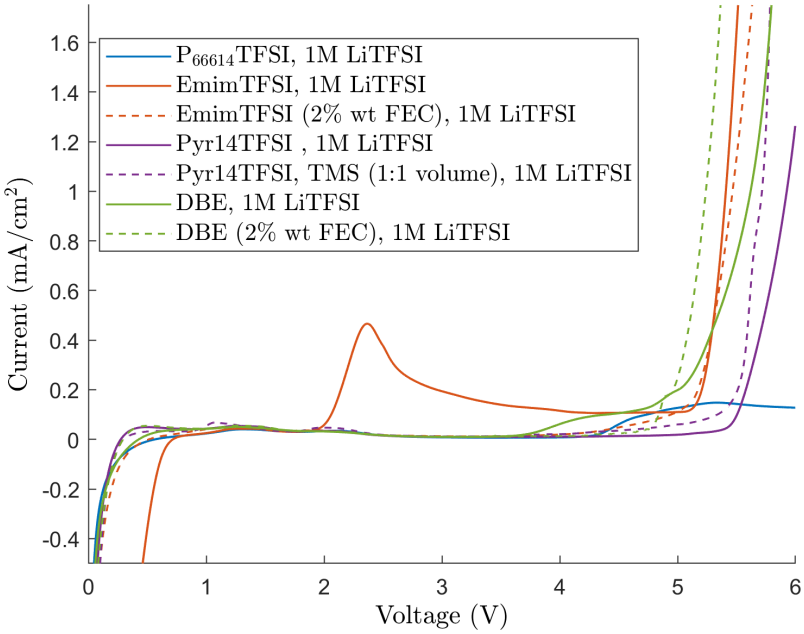

Figure 4.4: LSV of the electrolytes from 0 V to 6 V with a sweep rate of 5 mV/s.

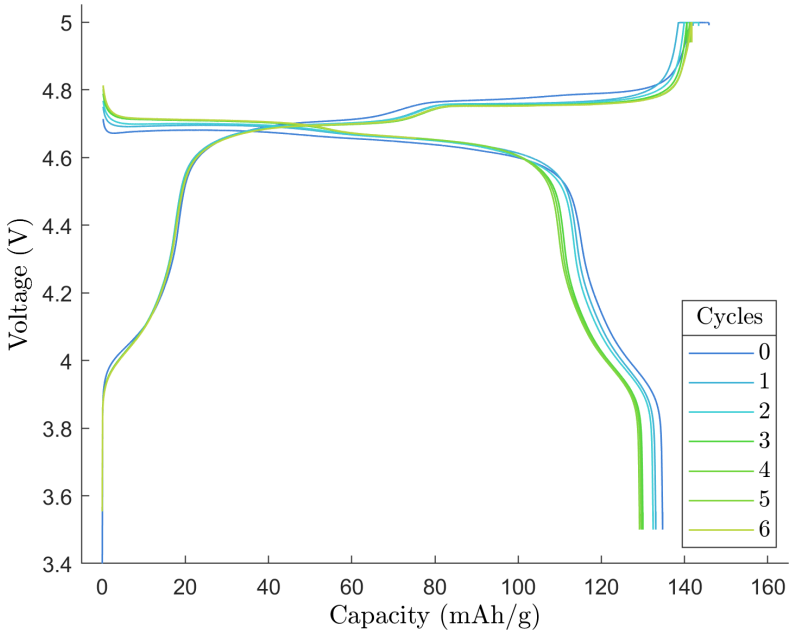

Figure 4.5: GC at a rate of C/10 of a Li/LNMO cell with 1 M LiTFSI in [PYR14][TFSI]:TMS (1:1).

The performance of DBE against G was also proved to be poor with a uneven charging curve indicating decomposition against the graphite anode, perhaps not being able to form a good SEI. However, when FEC was added, the performance improved (Fig. 4.6). The coulombic efficiency was however still very low and the capacity retention as well, with the cell only cycled for 13 cycles. To investigate the performance of a commercial electrolyte against a high-voltage cathode EC:DMC with 1M $LiPF_6$ was cycled in a LNMO/Li cell (Fig. 4.7). Ironically enough, it

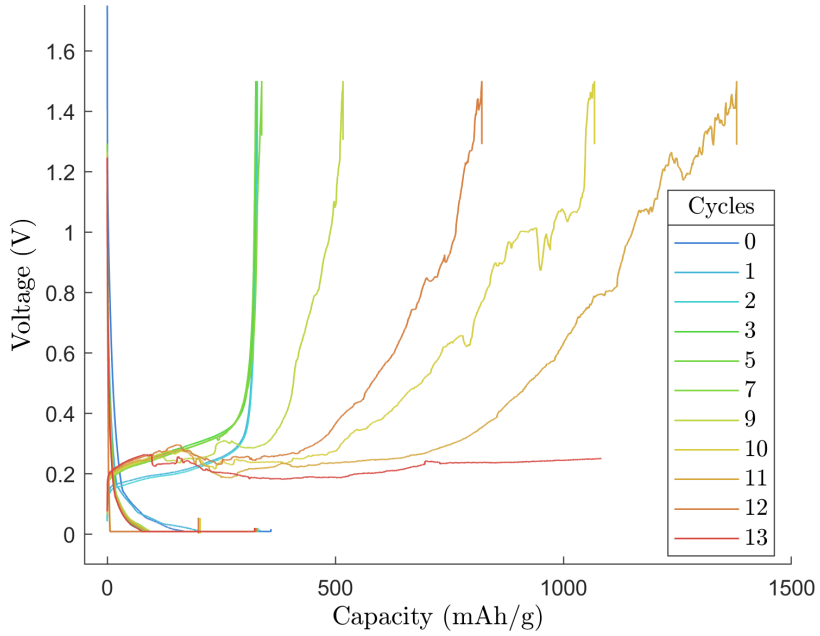

Figure 4.6: GC at a rate of C/10 of a Li/G cell with 1 M LiTFSI in DBE (2 % wt. FEC).

gave the best performance with high capacity retention over 25 cycles before being stopped. However, it is also important to take the elevated temperature of a commercial battery into consideration. The electrolyte might not be as stable in a stack configuration.

4.4.3 Dual electrolytes

After proving the cycling stability for 1 M LiTFSI in [PYR14][TFSI]:TMS (1:1) and 1 M LiTFSI in DBE (2% wt FEC) the pair was tested in the coin cell setup with the glass fibre separators as well as the Swagelok setup with the Teflon spacer. While both the separator (Fig. 4.8) and spacer setup (Fig. 4.9) looked promising from the beginning, with the characteristic charging bumps of [PYR14][TFSI] seen in Fig. 4.5 visible in both dual electrolyte cells. However, neither of the cells reaches the nominal voltage plateau, showing no signs of the intercalation of ions. A small bump is visible in the graph for the spacer, but it is unclear what the source of this is. A swagelok cell with LFP/G was also cycled, to be used as a comparison to the LNMO, seen in Fig. 4.10. Surprisingly enough, this cell could be cycled and showed high coulombic efficiency but low capacity. However, since the teflon spacer covered a large area of the electrode and the specific capacity was not adjusted, this is probably too low of a value.

4.5 Discussion

The results showed one cell being able to cycle in at least one dual electrolyte setup without separators. However, due to time constraints, only three LNMO

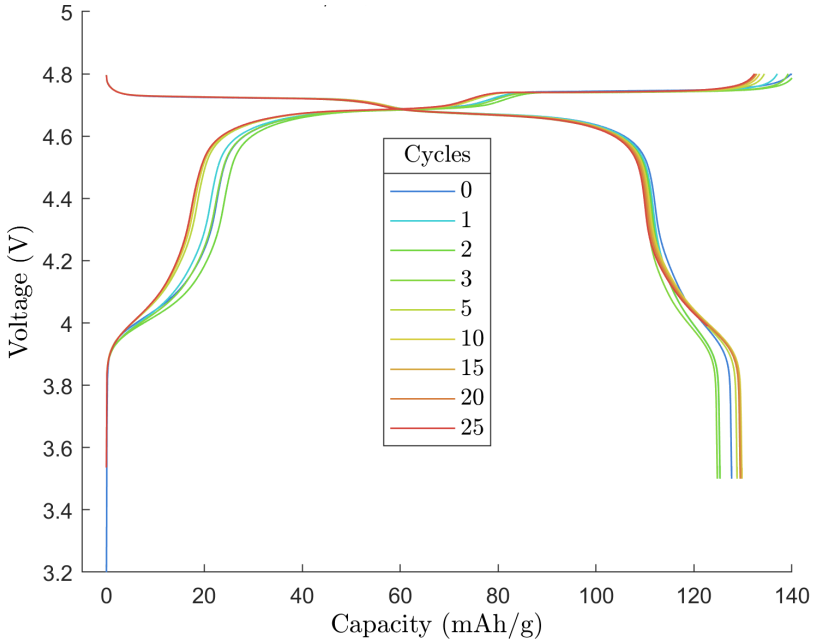

Figure 4.7: GC at a rate of C/10 of a Li/LNMO cell with the commercial electrolyte 1 M $LiPF_6$ in EC:DMC (1:1).

dual electrolytes were tested. Due to the peculiar stacking of the spacer cell, the problem simply might have been bad contact between the top electrode and the DBE. Further measurements need to be done to be able to confidently identify the LNMO as the problem. Given the good cycling performance of the [PYR14][TFSI] and TMS electrolyte against LNMO there are no apparent reasons why it did not work for this cell. Perhaps an exception being interactions between DBE and the lithium metal, in comparison with the graphite used for the LFP cell. Furthermore, given the few number of cells measured it is also hard to draw a conclusion about the failure of the separator cell. No clear signs of decomposition of the electrolyte was visible.

However, [PYR14][TFSI] together with TMS was proved to be a promising immiscible electrolyte pair, and the mobility of ions across the DBE (2% wt FEC) interface was proven to be adequate enough to cycle the LFP/G cell.

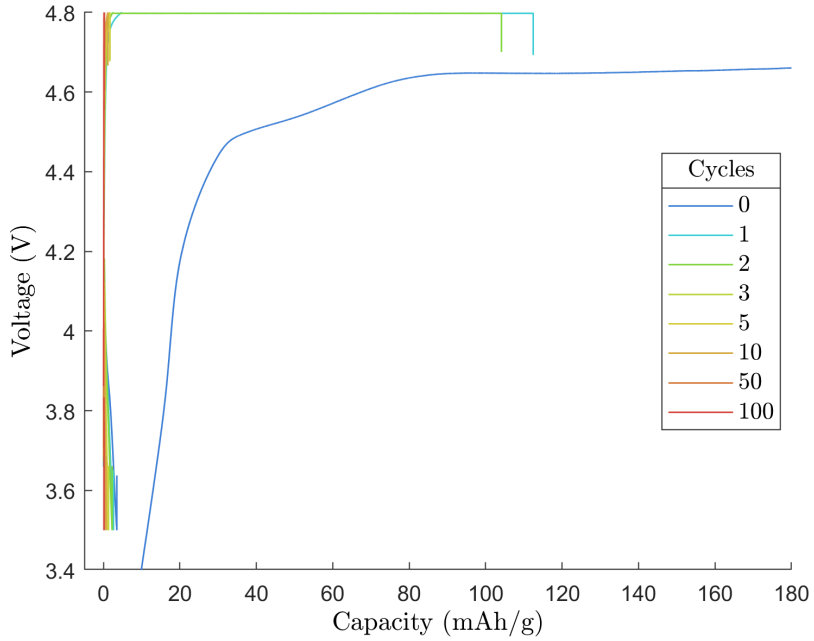

Figure 4.8: GC at a rate of C/10 of a G/LNMO dual electrolyte cell with 1 M LiTFSI in DBE (2 % wt. FEC) and 1 M LiTFSI in [PYR14][TFSI]:TMS (1:1). Two glass fibre separators were placed in the cell with the DBE and FEC in contact with the graphite, and the [PYR14][TFSI] and TMS in contact with the cathode.

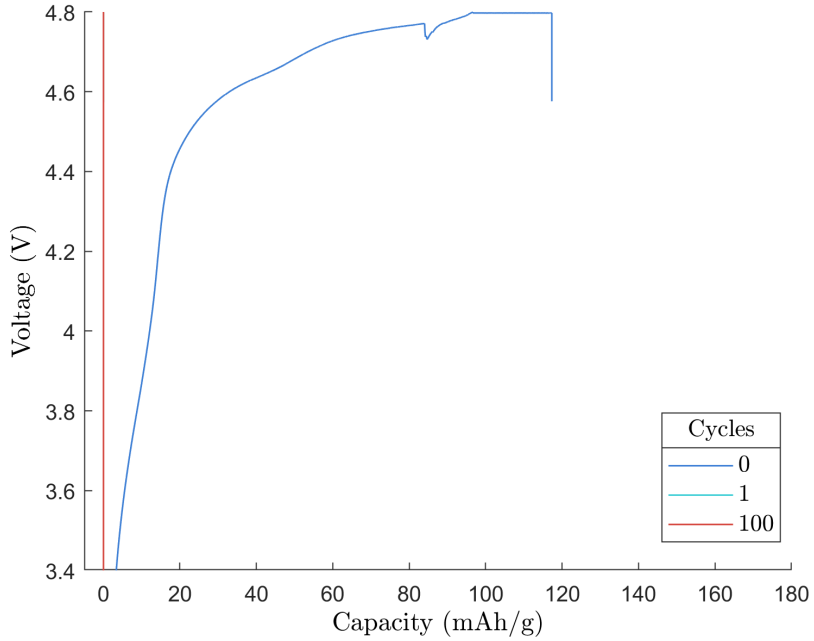

Figure 4.9: GC at a rate of C/10 of a G/LNMO dual electrolyte cell with 1 M LiTFSI in DBE (2 % wt. FEC) and 1 M LiTFSI in [PYR14][TFSI]:TMS (1:1). A Teflon spacer was used in a Swagelok cell to contain the electrolytes, with the DBE and FEC in contact with the graphite, and the [PYR14][TFSI] and TMS in contact with the cathode.

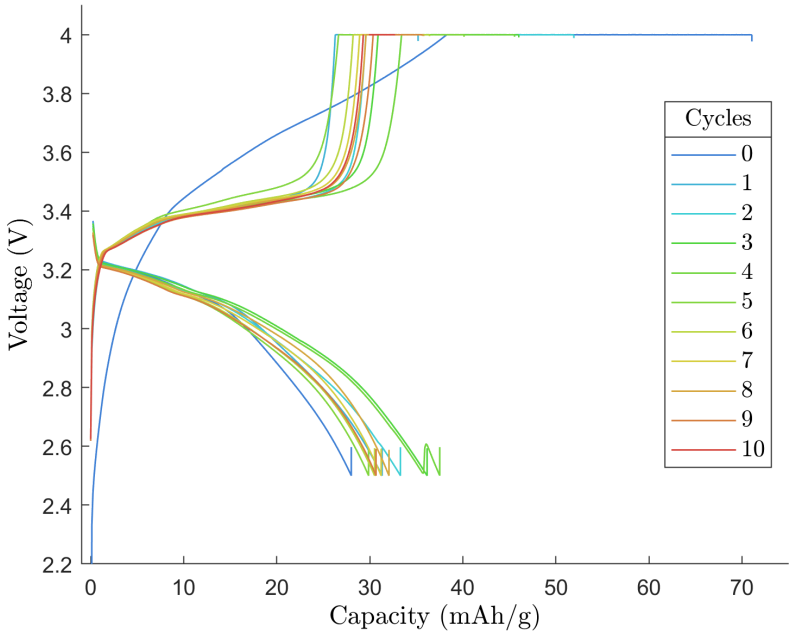

Figure 4.10: GC at a rate of C/10 of a G/LFP dual electrolyte Swagelok cell with 1 M LiTFSI in DBE (2 % wt. FEC) and 1 M LiTFSI in [PYR14][TFSI]:TMS (1:1).

5
Final remarks

New electrolyte concepts need to be developed to not hinder the potential of high voltage electrodes. Unfortunately, no single electrolyte inhabits all desired properties and therefore, new design concepts, combinations of electrolytes or novel cell setups. The aim of this thesis was to investigate the implementation of a dual electrolyte design as a method to extend the ESW of conventional electrolytes. The design was based on the chemical immscible electrolytes creating a barrier around its electrolyte, protecting it from parasitic reactions.

The thesis approached the design in two ways. Firstly, potential electrolytes, within the realm of battery research, were selected based on their immiscibility with another. Furthermore, in an effort to understand the mechanisms of electrolytes in porous battery separator, a high resolution characterisation technique was found in confocal Raman spectroscopy. By combining a characterisation cell already adapted for optical spectroscopy, a sample setup meant to emulate the conditions of a battery was created. Measurements on battery separators proved that it was possible to distinguish between molecular species on thicker glass fibre seprators, while the transparency of thin polymer separators meant the Raman signal was scattered throughout the sample, diluting the signal response. A more purposefully designed measurement setup, perhaps involving strongly Raman active materials, such as silicon, could bring the resolution down to a 1-50 μm level.

The electrolytes tested for their immiscibility were further characterised for their intended purpose in LIBs. While a few pair were sorted out due to their poor performance during small scale cycling with coin cells, the [PYR14][TFSI]/TMS versus DBE/FEC pairing proved promising during single electrolyte measurements. The few measurements with two separators of different electrolytes were unsuccessful but in a Swagelok setup with only liquids, the reliable cycling of a LFP cell could be proven. While the lack of separators in the cell creates issues in itself, namely making the cell more sensitive to movement, the promising electrochemical properties of this pair makes further research into the immiscible system relevant.

Bibliography

[1] N. Campagnol, A. Pfeiffer, and C. Tryggestad. (2022) Capturing the battery value-chain opportunity. [Online]. Available: https://www.mckinsey.com/industries/electric-power-and-natural-gas/our-insights/capturing-the-battery-value-chain-opportunity

[2] World Economic Forum, "A vision for a sustainable battery value chain in 2030," 2019. [Online]. Available: https://www.weforum.org/reports/a-vision-for-a-sustainable-battery-value-chain-in-2030/

[3] M. Grohol and C. Veeh, "Study on the Critical Raw Materials for the EU 2023 Final Report," 2023. [Online]. Available: https://single-market-economy.ec.europa.eu/publications/study-critical-raw-materials-eu-2023-final-report_en

[4] M. Li, J. Lu, Z. Chen, and K. Amine, "30 years of lithium-ion batteries," *Advanced Materials*, vol. 30, p. 1800561, 8 2018.

[5] K. W. Beard, *Linden's Handbook of Batteries*. McGraw-Hill Education, 2019, ch. SECTION A: LITHIUM-ION BATTERIES.

[6] J. T. Frith, M. J. Lacey, and U. Ulissi, "A non-academic perspective on the future of lithium-based batteries," *Nature Communications*, vol. 14, 12 2023.

[7] R. T. Jow, J. K. Xu, O. Borodin, and M. Ue, *Electrolytes for Lithium and Lithium-Ion Batteries*. Springer Science+Business Media, 2014. [Online]. Available: http://www.springer.com/series/6251

[8] Customcells Holding GmbH, "Technical data sheet: Lithium-iron-phosphate," 2022.

[9] C. P. Grey and D. S. Hall, "Prospects for lithium-ion batteries and beyond—a 2030 vision," *Nature Communications*, vol. 11, p. 6279, 12 2020.

[10] X. Fan and C. Wang, "High-voltage liquid electrolytes for Li batteries: progress and perspectives," *Chemical Society Reviews*, vol. 50, pp. 10 486–10 566, 2021.

[11] W. Li, B. Song, and A. Manthiram, "High-voltage positive electrode materials for lithium-ion batteries," *Chemical Society Reviews*, vol. 46, pp. 3006–3059, 2017.

[12] S. He, S. Huang, Y. Zhao, H. Qin, Y. Shan, and X. Hou, "Design of a Dual-Electrolyte Battery System Based on a High-Energy NCM811-Si/C Full Battery Electrode-Compatible Electrolyte," *ACS Applied Materials & Interfaces*, vol. 13, pp. 54 069–54 078, 11 2021.

[13] Y. Ding and G. Yu, "A bio-inspired, heavy-metal-free, dual-electrolyte liquid battery towards sustainable energy storage," *Angewandte Chemie International Edition*, vol. 55, pp. 4772–4776, 4 2016.

[14] Y. Ren and A. Manthiram, "A dual-phase electrolyte for high-energy lithium–sulfur batteries," *Advanced Energy Materials*, vol. 12, p. 2202566, 12 2022.

[15] S.-J. Cho, G. Y. Jung, S. H. Kim, M. Jang, D.-K. Yang, S. K. Kwak, and S.-Y. Lee, "Monolithic heterojunction quasi-solid-state battery electrolytes based on thermodynamically immiscible dual phases," *Energy & Environmental Science*, vol. 12, pp. 559–565, 2019.

[16] M. Winter, B. Barnett, and K. Xu, "Before li ion batteries," *Chemical Reviews*, vol. 118, pp. 11 433–11 456, 12 2018.

[17] K. W. Beard, *Linden's Handbook of Batteries*. McGraw-Hill Education, 2019, ch. PART 2: PRINCIPLES OF ELECTROCHEMICAL CELL OPERATIONS.

[18] K. Xu, *Electrolytes, Interfaces and Interphases: Fundamentals and Applications in Batteries*. The Royal Society of Chemistry, 2023.

[19] G. Li, "Regulating mass transport behavior for high-performance lithium metal batteries and fast-charging lithium-ion batteries," *Advanced Energy Materials*, vol. 11, p. 2002891, 2 2021.

[20] J. S. Kim, Z. Wu, A. R. Morrow, A. Yethiraj, and A. Yethiraj, "Self-diffusion and viscosity in electrolyte solutions," *The Journal of Physical Chemistry B*, vol. 116, pp. 12 007–12 013, 10 2012.

[21] A. V. Karatrantos, T. Ohba, and Q. Cai, "Diffusion of ions and solvent in propylene carbonate solutions for lithium-ion battery applications," *Journal of Molecular Liquids*, vol. 320, p. 114351, 12 2020.

[22] M. Winter, "The solid electrolyte interphase – the most important and the least understood solid electrolyte in rechargeable li batteries," *Zeitschrift für Physikalische Chemie*, vol. 223, pp. 1395–1406, 12 2009.

[23] E. Peled, "The electrochemical behavior of alkali and alkaline earth metals in nonaqueous battery systems—the solid electrolyte interphase model," *Journal of The Electrochemical Society*, vol. 126, pp. 2047–2051, 12 1979.

[24] F. Shi and P. N. Ross, "Solid electrolyte interphase in lithium-based batteries," *Encyclopedia of Inorganic and Bioinorganic Chemistry*, pp. 1–17, 3 2019.

[25] M. Gauthier, T. J. Carney, A. Grimaud, L. Giordano, N. Pour, H.-H. Chang, D. P. Fenning, S. F. Lux, O. Paschos, C. Bauer, F. Maglia, S. Lupart, P. Lamp, and Y. Shao-Horn, "Electrode–Electrolyte Interface in Li-Ion Batteries: Current Understanding and New Insights," *The Journal of Physical Chemistry Letters*, vol. 6, pp. 4653–4672, 11 2015.

[26] E. Peled and S. Menkin, "Review—sei: Past, present and future," *Journal of The Electrochemical Society*, vol. 164, pp. A1703–A1719, 6 2017.

[27] N. Mohamed and N. K. Allam, "Recent advances in the design of cathode materials for Li-ion batteries," *RSC Advances*, vol. 10, pp. 21 662–21 685, 2020.

[28] G. Pistoia, *Lithium-Ion Batteries: Advances and Applications*. Elsevier, 2014.

[29] W. Zhu, J. Zhang, J. Luo, C. Zeng, H. Su, J. Zhang, R. Liu, E. Hu, Y. Liu, W. Liu, Y. Chen, W. Hu, and Y. Xu, "Ultrafast non-equilibrium synthesis of cathode materials for li-ion batteries," *Advanced Materials*, vol. 35, p. 2208974, 1 2023.

[30] D. Linden, T. B. Reddy, and K. W. Beard, *Linden's Handbook of Batteries*. McGraw-Hill Education, 2019, ch. THEORETICAL ELECTROCHEMISTRY FUNDAMENTALS.

[31] F. Zou, H. C. Nallan, A. Dolocan, Q. Xie, J. Li, B. M. Coffey, J. G. Ekerdt, and A. Manthiram, "Long-life LiNi0.5Mn1.5O4/graphite lithium-ion cells with an artificial graphite-electrolyte interface," *Energy Storage Materials*, vol. 43, pp. 499–508, 12 2021.

[32] G. Ganas, G. Kastrinaki, D. Zarvalis, G. Karagiannakis, A. Konstandopoulos, D. Versaci, and S. Bodoardo, "Synthesis and characterization of LNMO cathode materials for lithium-ion batteries," *Materials Today: Proceedings*, vol. 5, pp. 27 416–27 424, 2018.

[33] J.-H. Kim, N. P. Pieczonka, Z. Li, Y. Wu, S. Harris, and B. R. Powell, "Understanding the capacity fading mechanism in LiNi0.5Mn1.5O4/graphite Li-ion batteries," *Electrochimica Acta*, vol. 90, pp. 556–562, 2 2013.

[34] R. Jung, P. Strobl, F. Maglia, C. Stinner, and H. A. Gasteiger, "Temperature Dependence of Oxygen Release from LiNi0.6Mn0.2Co0.2O (NMC622) Cathode Materials for Li-Ion Batteries," *Journal of The Electrochemical Society*, vol. 165, pp. A2869–A2879, 9 2018.

[35] B. L.-H. Hu, F.-Y. Wu, C.-T. Lin, A. N. Khlobystov, and L.-J. Li, "Graphene-modified LiFePO4 cathode for lithium ion battery beyond theoretical capacity," *Nature Communications*, vol. 4, p. 1687, 4 2013.

[36] L. Hu, Z. Zhang, and K. Amine, "Fluorinated electrolytes for Li-ion battery: An FEC-based electrolyte for high voltage LiNi0.5Mn1.5O4/graphite couple," *Electrochemistry Communications*, vol. 35, pp. 76–79, 10 2013.

[37] Customcells Holding GmbH, "Technical data sheet: Graphite," 2022.

[38] K. Xu, "Electrolytes and Interphases in Li-Ion Batteries and Beyond," *Chemical Reviews*, vol. 114, pp. 11 503–11 618, 12 2014.

[39] B. Rowden and N. Garcia-Araez, "Estimating lithium-ion battery behavior from half-cell data," *Energy Reports*, vol. 7, pp. 97–103, 5 2021.

[40] L. Lv, Y. Wang, W. Huang, Y. Wang, G. Zhu, and H. Zheng, "Effect of lithium salt type on silicon anode for lithium-ion batteries," *Electrochimica Acta*, vol. 413, p. 140159, 5 2022.

[41] G. Jiang, F. Li, H. Wang, M. Wu, S. Qi, X. Liu, S. Yang, and J. Ma, "Perspective on high-concentration electrolytes for lithium metal batteries," *Small Structures*, vol. 2, p. 2000122, 5 2021.

[42] Y. Liu, C. Zhao, J. Du, X. Zhang, A. Chen, and Q. Zhang, "Research progresses of liquid electrolytes in lithium-ion batteries," *Small*, vol. 19, p. 2205315, 2 2023.

[43] S. Chen, S. R. Jeong, and S. Tao, "Key materials and future perspective for aqueous rechargeable lithium-ion batteries," *Materials Reports: Energy*, vol. 2, p. 100096, 5 2022.

[44] L. Suo, O. Borodin, T. Gao, M. Olguin, J. Ho, X. Fan, C. Luo, C. Wang, and K. Xu, ""Water-in-salt" electrolyte enables high-voltage aqueous lithium-ion chemistries," *Science*, vol. 350, pp. 938–943, 11 2015.

[45] K. Xu, "Nonaqueous liquid electrolytes for lithium-based rechargeable batteries," *Chemical Reviews*, vol. 104, pp. 4303–4418, 10 2004.

[46] H. Liang, X. Zuo, L. Zhang, W. Huang, Q. Chen, T. Zhu, J. Liu, and J. Nan, "Nonflammable LiTFSI-Ethylene Carbonate/1,2-Dimethoxyethane Electrolyte for High-Safety Li-ion Batteries," *Journal of The Electrochemical Society*, vol. 167, p. 090520, 1 2020.

[47] X. Meng, P. Zheng, J. Wu, and Z. Liu, "Density and viscosity measurements of diethyl ether from 243 to 373k and up to 20mpa," *Fluid Phase Equilibria*, vol. 271, pp. 1–5, 10 2008.

[48] X. Meng, J. Wu, and Z. Liu, "Viscosity and density measurements of diisopropyl ether and dibutyl ether at different temperatures and pressures," *Journal of Chemical & Engineering Data*, vol. 54, pp. 2353–2358, 9 2009.

[49] B. Koo, H. Lee, S. Hwang, and H. Lee, "Ionic Conduction and Speciation in LiPF6 and LiBF4 Dimethyl Sulfoxide Electrolytes: Comparison with Propylene Carbonate Electrolytes," *The Journal of Physical Chemistry C*, vol. 127, no. 12, pp. 5676–5682, Mar 2023. [Online]. Available: https://doi.org/10.1021/acs.jpcc.2c08977

[50] A. Abouimrane, I. Belharouak, and K. Amine, "Sulfone-based electrolytes for high-voltage Li-ion batteries," *Electrochemistry Communications*, vol. 11, no. 5, pp. 1073–1076, 2009. [Online]. Available: https://www.sciencedirect.com/science/article/pii/S1388248109001374

[51] M. Watanabe, M. L. Thomas, S. Zhang, K. Ueno, T. Yasuda, and K. Dokko, "Application of ionic liquids to energy storage and conversion materials and devices," *Chemical Reviews*, vol. 117, pp. 7190–7239, 5 2017.

[52] K. Karuppasamy, J. Theerthagiri, D. Vikraman, C.-J. Yim, S. Hussain, R. Sharma, T. Maiyalagan, J. Qin, and H.-S. Kim, "Ionic liquid-based electrolytes for energy storage devices: A brief review on their limits and applications," *Polymers*, vol. 12, p. 918, 4 2020.

[53] G. B. Appetecchi, M. Montanino, A. Balducci, S. F. Lux, M. Winterb, and S. Passerini, "Lithium insertion in graphite from ternary ionic liquid-lithium salt electrolytes: I. electrochemical characterization of the electrolytes," *Journal of Power Sources*, vol. 192, no. 2, pp. 599–605, 2009. [Online]. Available: https://www.sciencedirect.com/science/article/pii/S0378775308024907

[54] Solvionic, "1-ethyl-3-methylimidazolium bis(trifluoromethanesulfonyl)imide," 2023. [Online]. Available: https://en.solvionic.com/products/1-ethyl-3-methylimidazolium-bistrifluoromethanesulfonylimide-99

[55] M. Hayyan, F. S. Mjalli, M. A. Hashim, I. M. AlNashef, and T. X. Mei, "Investigating the electrochemical windows of ionic liquids," *Journal of Industrial and Engineering Chemistry*, vol. 19, no. 1, pp. 106–112, 2013. [Online]. Available: https://www.sciencedirect.com/science/article/pii/S1226086X12002353

[56] Solvionic, "1-butyl-1-methylpyrrolidinium bis(trifluoromethanesulfonyl)imide," 2023. [Online]. Available: https://en.solvionic.com/products/1-butyl-1-methylpyrrolidinium-bistrifluoromethanesulfonylimide-99.9

[57] Iolitec Ionic Liquids Technologies GmbH. (2023) Trihexyltetradecylphosphonium bis(trifluoromethylsulfonyl)imide. [Online]. Available: https://iolitec.de/en/node/328

[58] J. Li, H. Zhu, C. Peng, and H. Liu, "Densities and viscosities for ionic liquids [BMIM][BF4] and [BMIM][Cl] and their binary mixtures at various temperatures and atmospheric pressure," *Chinese Journal of Chemical Engineering*, vol. 27, no. 12, pp. 2994–2999, 2019. [Online]. Available: https://www.sciencedirect.com/science/article/pii/S1004954119300606

[59] H. Wang, S. Liu, K. Huang, X. Yin, Y.-N. Liu, and S. Peng, "BMIMBF4 Ionic Liquid Mixtures Electrolyte for Li-ion Batteries," *International Journal Of Electrochemical Science*, vol. 7, pp. 1688–1698, 02 2012.

[60] A. Smith, P. Stüble, L. Leuthner, A. Hofmann, F. Jeschull, and L. Mereacre, "Potential and limitations of research battery cell types for electrochemical data acquisition," *Batteries & Supercaps*, 4 2023.

[61] Z. Samec, "Electrochemistry at the interface between two immiscible electrolyte solutions (IUPAC Technical Report)," *Pure and Applied Chemistry*, vol. 76, pp. 2147–2180, 1 2004.

[62] C. V. Amanchukwu, X. Kong, J. Qin, Y. Cui, and Z. Bao, "Nonpolar alkanes modify lithium-ion solvation for improved lithium deposition and stripping," *Advanced Energy Materials*, vol. 9, p. 1902116, 11 2019.

[63] National Center for Biotechnology Information. (2023) Pubchem compound summary for cid 8071, 1,2-dimethoxyethane. [Online]. Available: https://pubchem.ncbi.nlm.nih.gov/compound/1_2-Dimethoxyethane

[64] ——. (2023) PubChem Compound Summary for CID 6228, N,N-Dimethylformamide. [Online]. Available: https://pubchem.ncbi.nlm.nih.gov/compound/N_N-Dimethylformamide.

[65] A. Arce, M. J. Earle, S. P. Katdare, H. Rodríguez, and K. R. Seddon, "Mutually immiscible ionic liquids," *Chem. Commun.*, pp. 2548–2550, 2006. [Online]. Available: http://dx.doi.org/10.1039/B604595B

[66] P. Vandenabeele, *Practical Raman Spectroscopy : An Introduction*. John Wiley & Sons, Ltd, 2013.

[67] C. Juang, L. Finzi, and C. J. Bustamante, "Design and application of a computer-controlled confocal scanning differential polarization microscope," *Review of Scientific Instruments*, vol. 59, pp. 2399–2408, 11 1988.

[68] E. J. F. Cedeño, "Development of operando diagnostics for Li-ion cathodes by Raman spectroscopy," 2019.

[69] "Confocal raman microspectroscopy: Theory and application to thin polymer samples," *Applied Spectroscopy*, vol. 46, pp. 60–68, 1 1992.

[70] N. J. Everall, "Confocal raman microscopy: Performance, pitfalls, and best practice," *Applied Spectroscopy*, vol. 63, pp. 245A–262A, 9 2009.

[71] V. Mazet. (2023) Background correction, matlab central file exchange. [Online]. Available: https://www.mathworks.com/matlabcentral/fileexchange/27429-background-correction

[72] X. Yang and A. L. Rogach, "Electrochemical techniques in battery research: A tutorial for nonelectrochemists," *Advanced Energy Materials*, vol. 9, no. 25, p. 1900747, 2019. [Online]. Available: https://onlinelibrary.wiley.com/doi/abs/10.1002/aenm.201900747

[73] A. J. Bard, L. R. Faulkner, and H. S. White, *Electrochemical Applications: Fundamentals and Applications*. John Wiley & Sons, Ltd, 2022.

[74] A. Mathew, M. J. Lacey, and D. Brandell, "Investigating oxidative stability of lithium-ion battery electrolytes using synthetic charge-discharge profile voltammetry," *Journal of Power Sources Advances*, vol. 11, p. 100071, 2021. [Online]. Available: https://www.sciencedirect.com/science/article/pii/S2666248521000263

[75] N. Salem, S. Zavorine, D. Nucciarone, K. Whitbread, M. Moser, and Y. Abu-Lebdeh, "Physical and electrochemical properties of some phosphonium-based ionic liquids and the performance of their electrolytes in lithium-ion batteries," *Journal of The Electrochemical Society*, vol. 164, no. 8, p. H5202, may 2017. [Online]. Available: https://dx.doi.org/10.1149/2.0061708jes

A

Additional cell cycling data

A number of coin cells with the selected electrolytes from the immiscibility studies were cycled galvanostatically, with varying performance.

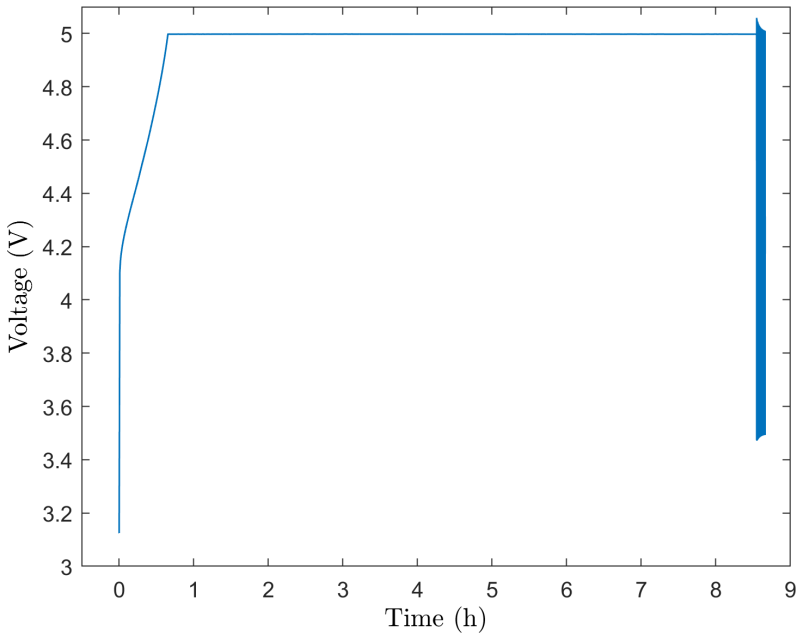

Figure A.1: GC at a rate of C/10 of a Li/LNMO cell with 1 M LiTFSI in $[P_{66614}][TFSI]$.

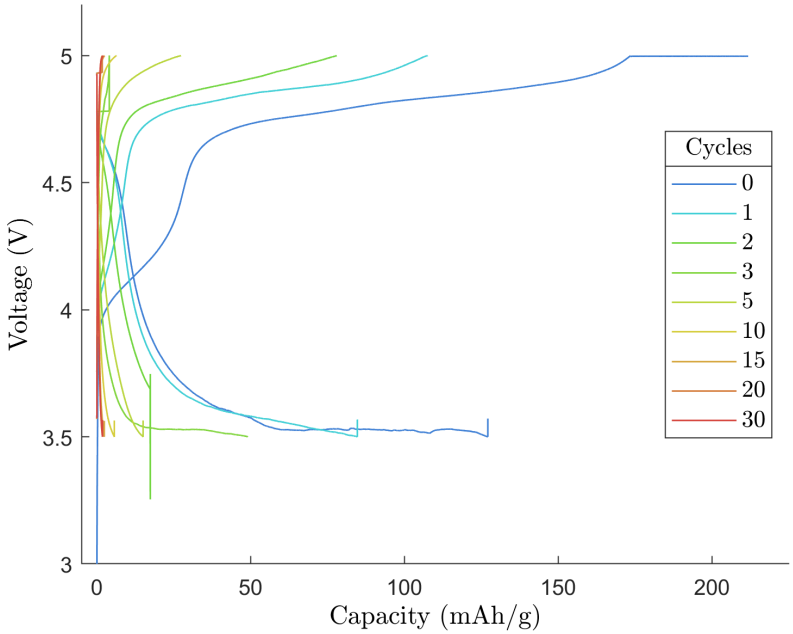

Figure A.2: GC at a rate of C/10 of a Li/LNMO cell with 1 M LiTFSI in [Emim][TFSI].

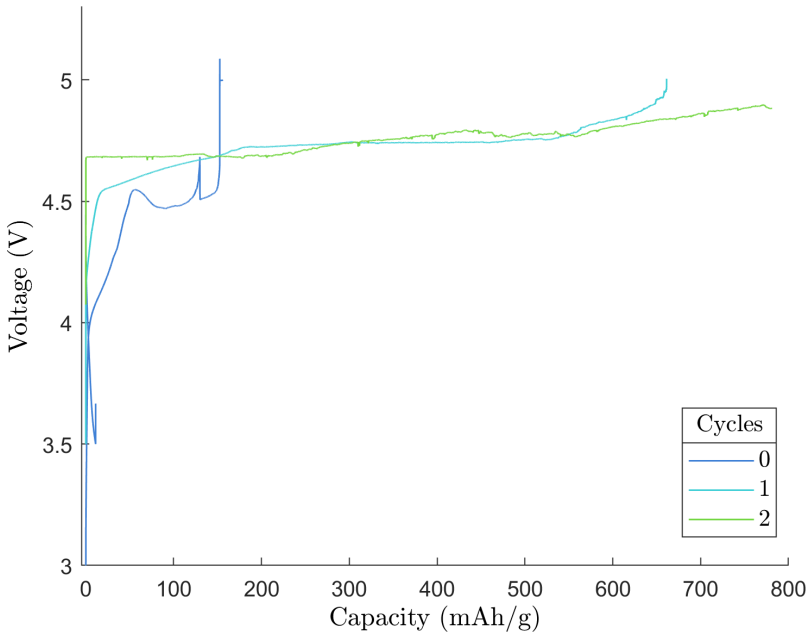

Figure A.3: GC at a rate of C/10 of a Li/LNMO cell with 1 M LiTFSI in DBE.

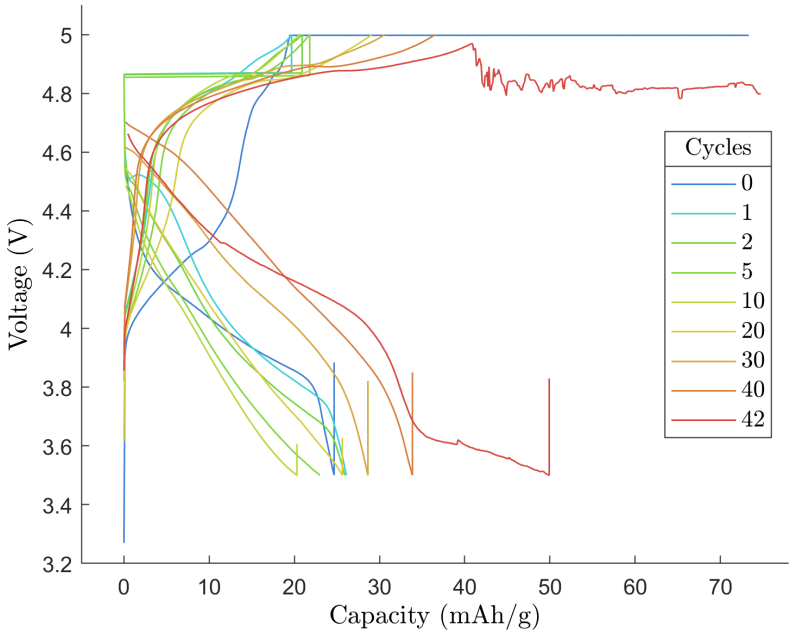

Figure A.4: GC at a rate of C/10 of a Li/LNMO cell with 1 M LiTFSI in [PYR14][TFSI].

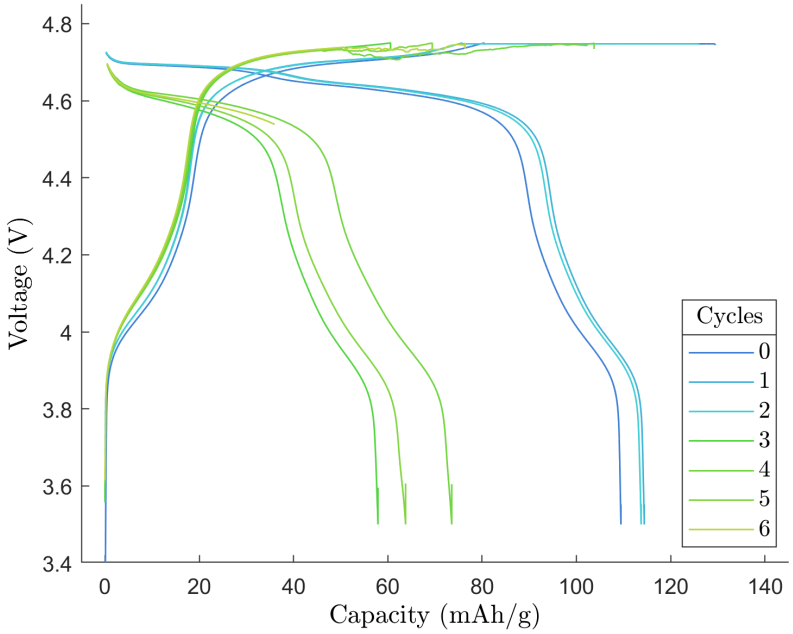

Figure A.5: GC at a rate of C/10 and 60°C of a Li/LNMO cell with 1 M LiTFSI in [PYR14][TFSI].

DEPARTMENT OF PHYSICS
CHALMERS UNIVERSITY OF TECHNOLOGY
Gothenburg, Sweden
www.chalmers.se

CHALMERS
UNIVERSITY OF TECHNOLOGY